

Article

The Genetic Association between Quartz Vein- and Greisen-Type Mineralization at the Maoping W–Sn Deposit, Southern Jiangxi, China: Insights from Zircon and Cassiterite U–Pb Ages and Cassiterite Trace Element Composition

Li-Li Chen, Pei Ni *, Bao-Zhang Dai *, Wen-Sheng Li, Zhe Chi and Jun-Yi Pan

State Key Laboratory for Mineral Deposits Research, Institute of Geo-Fluids, School of Earth Sciences and Engineering, Nanjing University, Nanjing 210023, China

* Correspondence: peini@nju.edu.cn (P.N.); daibz@nju.edu.cn (B.-Z.D.); Tel.: +86-25-8968-0883 (P.N.); +86-25-8368-6649 (B.-Z.D.)

Received: 28 May 2019; Accepted: 3 July 2019; Published: 4 July 2019



Abstract: The large-scale Maoping W–Sn deposit in the Gannan metallogenic belt of the eastern Nanling Range, South China, spatially associated with the Maoping granite pluton, hosts total ore reserves of 103,000 t WO₃ and 50,000 t Sn. Two different types of mineralization developed in this deposit: Upper quartz vein-type mineralization, mostly within the Cambrian metamorphosed sandstone and slate, and underneath greisen-type mineralization within the Maoping granite. Cassiterites from both types of mineralization coexist with wolframite. Here we report for the first time in situ U–Pb data on cassiterite and zircon of the Maoping deposit obtained by LA-ICP-MS. Cassiterite from quartz vein and greisen yielded weighted average ²⁰⁶Pb/²³⁸U ages of 156.8 ± 1.5 Ma and 156.9 ± 1.4 Ma, respectively, which indicates that the two types of mineralization formed roughly at the same time. In addition, the two mineralization ages are consistent with the emplacement age of the Maoping granite (159.0 ± 1.5 Ma) within error, suggesting a close temporal and genetic link between W–Sn mineralization and granitic magmatism. The two types of mineralization formed at the same magmatic-hydrothermal event. Cassiterite from both types of mineralization shows high Fe, Ta, and Zr contents with a low Zr/Hf ratio, suggesting that the ore-forming fluid should be derived from the highly differentiated Maoping granite pluton. Cassiterite in greisen has higher contents of Nb and Ta but a lower concentration of Ti compared with that in quartz vein, indicating that the formation temperature of greisen-type mineralization is little higher than that of quartz-vein-type mineralization.

Keywords: cassiterite U–Pb dating; zircon U–Pb dating; trace element; Maoping W–Sn deposit; South China

1. Introduction

China accounts for 65% and 29% of the global total tungsten and tin reserves, respectively [1,2]. The Nanling metallogenic belt in south China is the most important tungsten and tin production region, accounting for approximately 83% of tungsten resources and 63% of tin resources of China [3]. The Gannan metallogenic belt (Figure 1A), as the eastern part of the Nanling metallogenic belt, is characterized by large-scale tungsten mineralization and contains 1.42 Mt of proven tungsten resources, which quartz vein-type tungsten deposits dominate [4]. Prospecting work uncovered greisen-type tungsten ore bodies in the granite at the bottom of the quartz vein-type tungsten ore bodies. Major W–Sn mineralization is commonly associated with highly differentiated and evolved granites [5,6]. The granite intrusions related to W–Sn deposits in the Gannan metallogenic belt occurred in multiple

stages (or episodes), including the Silurian (410–440 Ma), Late Triassic (230–210 Ma), Mid–Late Jurassic (170–150 Ma), and Cretaceous (134–80 Ma) [7–9]. Previous studies yielded age constraints on W–Sn mineralization in the Gannan metallogenic belt using K–Ar, ^{40}Ar – ^{39}Ar , Sm–Nd, and Rb–Sr dating of whole-rock/mineral [10–12] and Re–Os dating of molybdenite [8,13]. These dated minerals, however, may not have temporal and genetic relationships to W–Sn deposition and/or may have been subjected to a disturbance in their isotopic system due to later hydrothermal alteration and thermal events. Due to the lack of accurate ore- and rock-forming chronology data, it is still controversial whether the quartz vein-type tungsten ore bodies and greisen-type tungsten ore bodies in the same deposit are the different forms of the same magma–hydrothermal–mineralization [4,14–16].

The Maoping W–Sn deposit, which is spatially associated with the Maoping granite and was discovered in the 1980s, is located within the Gannan metallogenic belt, South China. Two types of mineralization developed in this deposit: Upper quartz vein-type W–Sn mineralization, mostly within the Cambrian metamorphosed rock, and underneath greisen-type W–Sn mineralization within the granite. Cassiterites from both types of mineralization coexist with wolframite. Accordingly, the Maoping deposit is a typical deposit for studying the relationship between quartz vein- and greisen-type mineralization. Previous geochronological studies on W–Sn mineralization in Maoping deposit have based on molybdenite Re–Os dating [8,17,18]. Molybdenite from hydrothermal Sn deposits is low in Re but high in common Os content, and a Re–Os isotopic system can occasionally have lost Re during later thermal events, with further loss during weathering [19]. The Maoping W–Sn deposit has two different mineralization types; and, based on Molybdenite Re–Os ages, it remains controversial whether they are contemporaneous or not. Therefore, in order to obtain accurate W–Sn mineralization age, it is preferable to use ore minerals to perform the dating. In addition, precise dating of the Maoping granite pluton has been lacking prior to this study. Whole-rock Sm–Nd dating was performed by Li [18]; however, although Sm–Nd systems are usually resistant to hydrothermal alteration [20], the obtained Sm–Nd age value of the Maoping granite (162 ± 22 Ma) contained a significant experimental error. Thus, the genetic relationship between the two types of mineralization and the Maoping granite pluton remains unclear.

Precise and accurate dating of the mineralization and granite pluton is critical for understanding: (i) the temporal relationship between quartz vein- and greisen-type mineralization; and (ii) the genetic relationship between the two types of mineralization and granitic magmatism. Cassiterite (ideally SnO_2) is one of the main ore minerals in a W–Sn deposit and generally has ppm-level U but low common Pb content [21,22]. Due to its refractory properties, cassiterite is resistant to later hydrothermal disturbances [23,24]. The U–Pb isotopic closure temperature of cassiterite with grain size of 1 μm can reach up to 560 °C [25], and most hydrothermal cassiterites are formed at under 500 °C (commonly at 200–400 °C) [26–28]. Therefore, U–Pb dating of cassiterite is an ideal method for directly obtaining the mineralization ages of W–Sn deposits [9,21,22,29–33]. Studies that couple cassiterite and zircon U–Pb dating make it possible to identify the relationship between W–Sn mineralization and the Maoping granite. In addition, due to its tetragonal lattice structure that is similar to that of rutile, cassiterite can incorporate a wide range of trace elements, including Nb, Ta, Zr, Hf, Ti, W, Fe, which can reflect the growth environment by recording primary physical and chemical information on the ore-forming fluids [24,34].

Cassiterite and zircon U–Pb dating has not yet been attempted for the Maoping deposit. Here, we combine the zircon and cassiterite U–Pb dating techniques to constrain the timing of granitic magmatism and the two different types of mineralization in the Maoping deposit. We then determine whether or not the two different types of mineralization are the products of the same magma–hydrothermal mineralization event.

2. Regional Geological Setting

The Gannan metallogenic belt is located within the eastern part of the Nanling metallogenic belt in the South China Block. The South China Block is composed of the Cathaysian Block to the Southeast

and the Yangtze Block to the Northwest, which are separated by the Shi–Hang Zone (Figure 1A). During the Neoproterozoic, tectonic processes resulted in amalgamation of the two blocks [35,36]. Metallogenesis in the Yanshanian period (Jurassic to early Cretaceous, 200–90 Ma) is associated with major tectono-thermal events that formed NE–SW trending faults and pluton emplacements [37,38].

Exposed rocks in the Gannan metallogenetic belt span the interval from Sinian to Quaternary, excluding the Silurian. Three rock series can be distinguished by Lithostratigraphic relationships: The Sinian to Ordovician metamorphic basement; Devonian to Permian shallow marine carbonate and siliclastic sedimentary cover; and Jurassic to Quaternary volcanoclastics and terrigenous red-bed sandstones (Figure 1B). The widespread Sinian to Ordovician basement and also the Devonian strata contain high concentrations of tungsten (up to 12 times the Clarke value) and are generally considered to be the source beds to the Yanshanian granite-related W and/or Sn deposits [39,40].

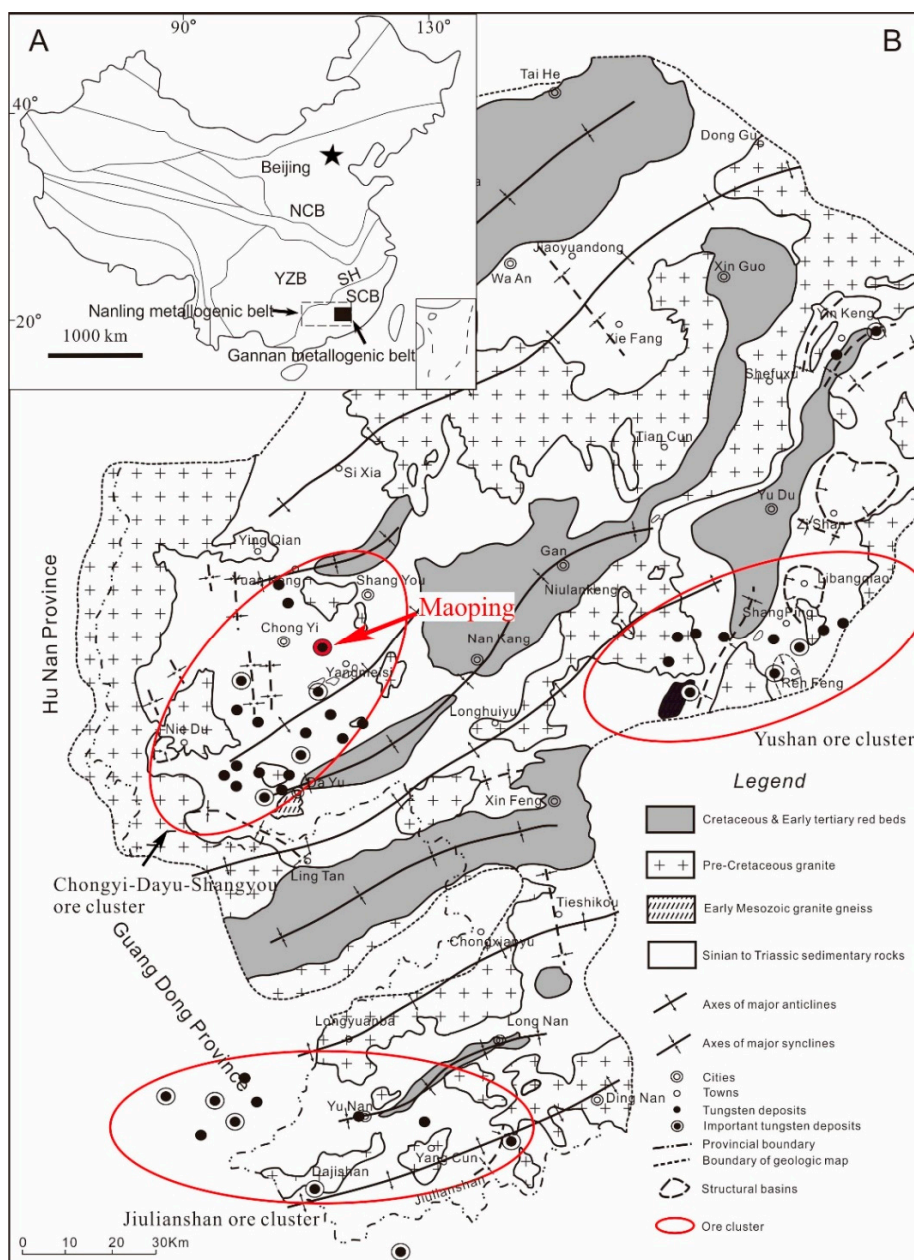


Figure 1. (A) A schematic tectonic map of China and the location of the Gannan metallogenetic belt and the Nanling metallogenetic belt; (B) the geology and distribution of the ore deposits in the Gannan metallogenetic belt and the location of the Maoping tungsten deposit (modified from [41]).

The main folding events in the Gannan metallogenic belt took place in the Early Paleozoic, the Triassic, and the Late Jurassic [41]. The early folds generally trend NNW or N, whereas the later folds generally trend ENE or NE (Figure 1B). In addition, there are two groups of E–W and NNE–SWW trending fault belts in this region. The EW-trending fault belts formed in Early Paleozoic and were reactivated in Jurassic. The NNE-trending fault belts formed in Jurassic. The Jurassic granites and related tungsten mineralization occur within the intersections of the EW- and NNE-trending fault belts [40].

In the Gannan metallogenic belt, a significant number of granitic plutons (about 500) outcrop and occupy a surface area of ca. 14,000 km². Two major magmatic events have been recognized: The Caledonian event (Early Paleozoic) and the Yanshanian event (Late Mesozoic) (Figure 1B). The Yanshanian event represents the most important period of magmatic activity, and its corresponding intrusions account for 68% of the total intrusions by area [42]. Almost all of the polymetallic tungsten and tin deposits in the Gannan metallogenic belt are associated with the Yanshanian granites, and occur at the endo- and exo-contact of the granite intrusions. The Yanshanian granites are mainly monzogranite or porphyritic monzogranite, composed of quartz (25%), K-feldspar and plagioclase (27–42%) with a K-feldspar/plagioclase ratio of > 1, and minor biotite. The accessory minerals are zircon, titanite, apatite, fluorite, topaz, and ilmenite. Geochemically, the granites contain SiO₂ > 68%, with K₂O > Na₂O, alkaline content >8%, and A/CNK > 1.1, thus corresponding to calc-alkaline granites. Granites genetically related to tungsten–tin mineralization commonly exhibit greisenization, potassic feldspathization, and albitization, or have fluorite alteration in the upper part of the granite [43,44].

Most of the tungsten deposits in South China are located in the Gannan metallogenic belt and surrounding regions. By 2007, 78 tungsten deposits and approximately 400 tungsten prospects had been found, including eight large, 24 medium, and 46 small deposits with a total WO₃ reserve of 1.7 Mt [42]. Various types of W–Sn mineralization have been recognized in the Gannan metallogenic belt, including quartz vein, altered granite, greisen, skarn, strata-bound and fracture zone [45]. Of these, quartz vein-type deposits contain the largest reserves and are mainly distributed in the Chongyi–Dayu–Shangyou, Jiulianshan and Yushan ore clusters. The Maoping deposit is located within the Chongyi–Dayu–Shangyou ore cluster (Figure 1B).

3. Geology of the Maoping W–Sn Deposit

Maoping, with mineralized area of about 2 km², is one of the largest W–Sn deposits in the Chongyi–Dayu–Shangyou ore cluster, which also hosts the world-class Xihuashan deposit [46,47]. Two types of orebodies were discovered and have been explored in this deposit: quartz vein-type orebodies and greisen-type orebodies. The quartz vein-type orebodies host 63,000 t of WO₃ and 15,000 t of Sn with average grades of 0.97% WO₃ and 0.30% Sn. The greisen-type orebodies host 40,000 t of WO₃ and 35,000 t of Sn with average grades of 0.18% WO₃ and 0.23% Sn [8]. The exposed strata of the mining areas consist mainly of Middle-Lower Cambrian low-grade metamorphosed sandstone and slate (Figure 2). Under the influence of the region's structure, folds and faults are well-developed in the mining area. The major folds include the Maoping homocline and the Shenfuxi–Gaoqiaoxia anticline, which have ~N–S axes that are approximately parallel with the major fold axes in the Gannan metallogenic belt. The principal ore-controlling faults strike E–W and dip S or N at 50–75°, which are 300–500 m long and several tens of cm wide. The post-mineralization faults are two reverse faults that strike NE and NW, respectively.

Intrusive rocks in the Maoping W–Sn deposit include a few exposed porphyritic veins and a buried granite pluton that was discovered during exploration (Figures 2 and 3). The porphyrite veins are cut through by ore veins and are pre-mineralization intrusions. The hidden granite pluton occurs over an area of 0.5 km², with the top elevation close to sea level. The Maoping granite extends in the E–W direction, and is comprised of medium–coarse-grained Fe–Li micas granite and fine-grained Fe–Li micas granite (Figure 4). The rock-forming minerals of medium–coarse-grained granite comprise quartz (35%–40%), plagioclase (30%–35%), K-feldspar (25%–30%), and Fe–Li mica (1%–5%). The major

accessory minerals are zircon, monazite, fluorite, apatite, and topaz. The rock-forming mineral content of the fine-grained Fe–Li micas granite is similar to that of the medium–coarse-grained Fe–Li micas granite, except for the micas. Quartz vein-type W–Sn mineralization occurs at the upper levels, whereas deeper greisen-type W–Sn mineralization occurs at the top of the granite pluton (Figure 3).

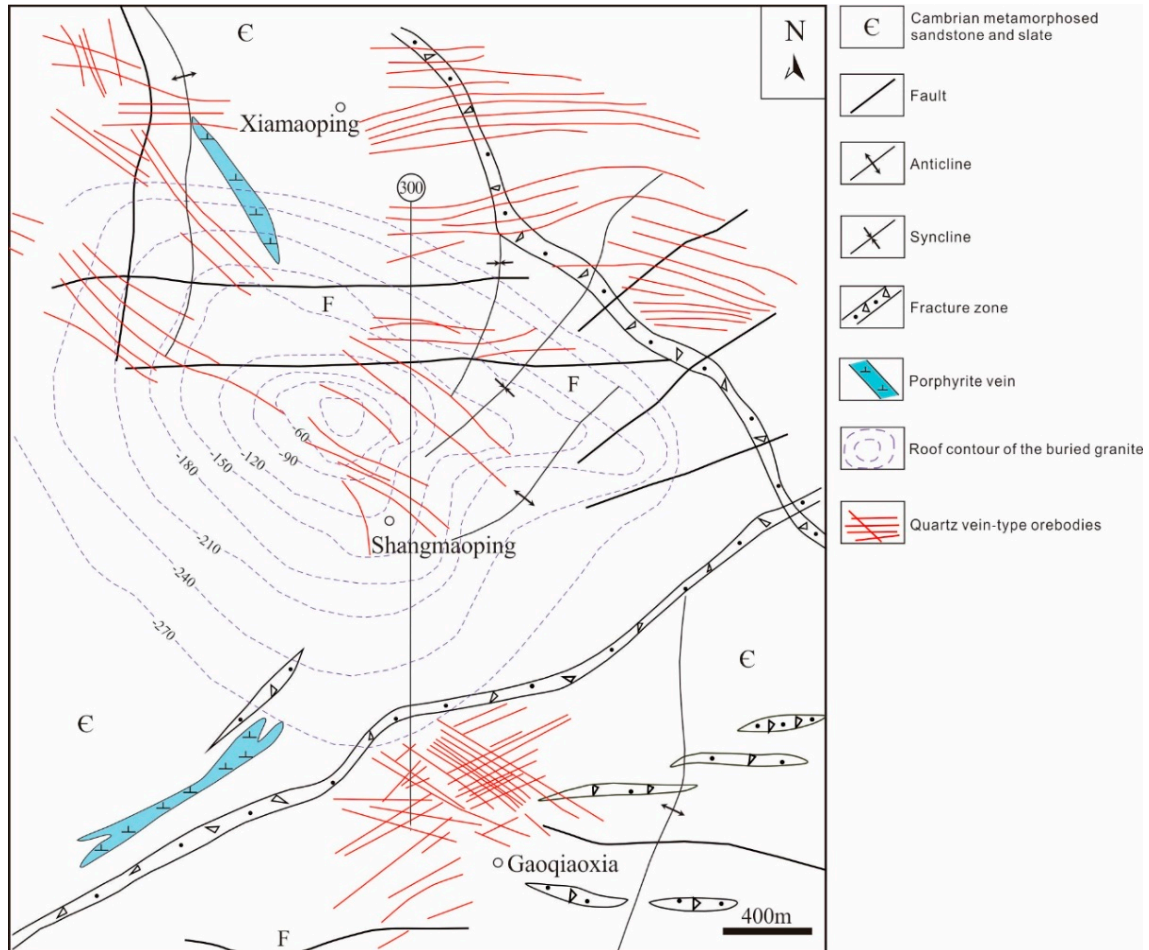


Figure 2. A schematic geological map of the Maoping tungsten deposit (modified from [48]).

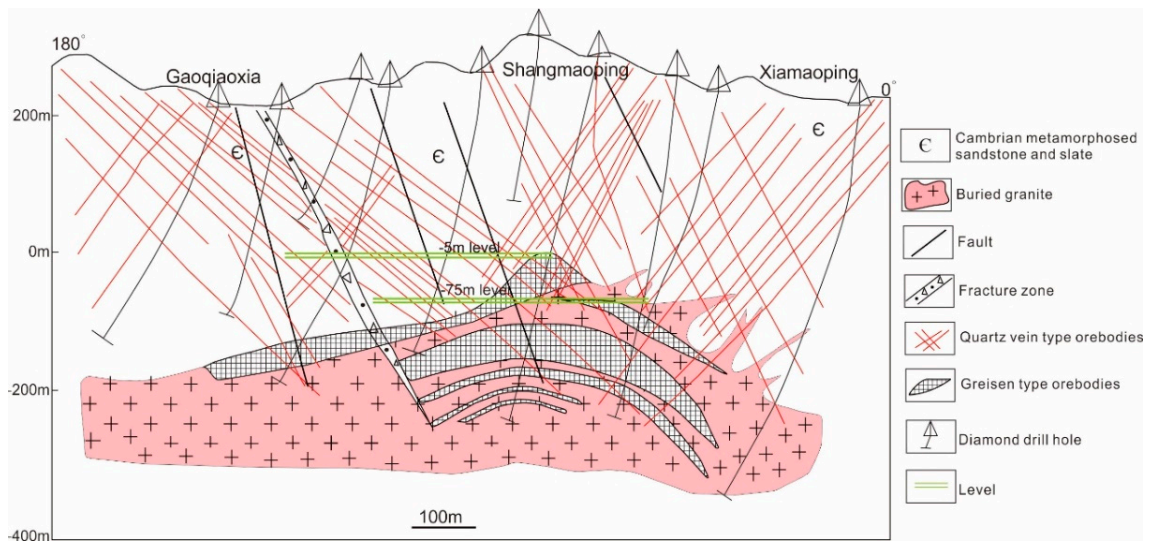


Figure 3. A geologic section in the Maoping tungsten deposit. See line 300 in Figure 2 (modified from [48]).

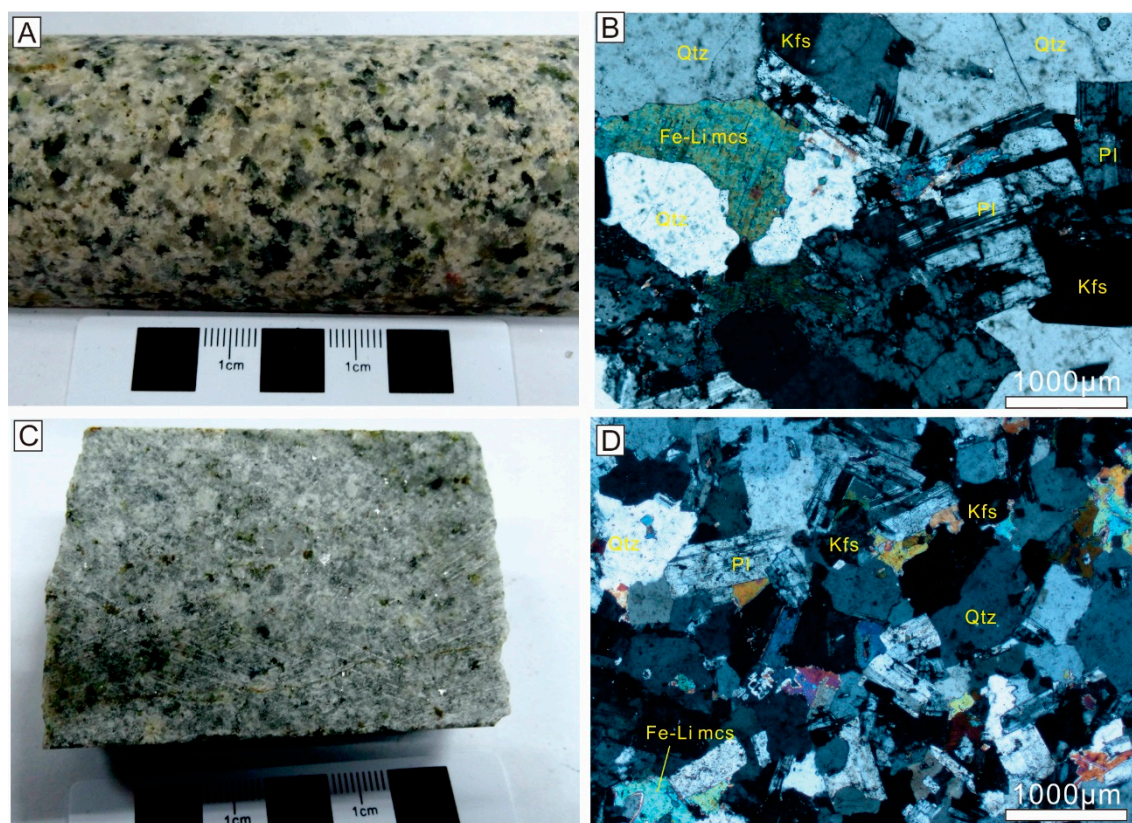


Figure 4. Photographs of granite samples from the Maoping W-Sn deposit. **A** and **B**, medium-coarse-grained Fe-Li micas granite (sample Zk30015-19); **C** and **D**, fine-grained Fe-Li micas granite (sample Zk30015-23). Fe-Li mcs, Fe-Li micas; Kfs, K-feldspar; Pl, plagioclase; Qtz, quartz.

The quartz vein-type orebodies (Figures 2 and 3) contain >400 individual ore veins that are commonly 300–400 m long and 10–30 cm wide, with the largest being over 60 cm in width. The ore veins are mostly hosted in the metamorphosed host rocks and less amounts in the cupola of the concealed granitic pluton. Wolframite coexisting with cassiterite are located at the edge of the vein body (Figure 5A,B). By considering the orientation and location of different ore veins, the Maoping deposit can be subdivided into the Xiamaping segment, the Shangmaoping segment, and the Gaoqiaoxia segment (Figure 3). Veins in the Xiamaping segment strike E–W or NW and dip to the S at 40–60°. Four groups of veins have been identified in the Shangmaoping segment. Veins that strike E–W dip to the N at 50–82°, whereas veins striking WNW, ~E–W, and NW are steep and have variable dip directions. Veins in the Gaoqiaoxia segment strike E–W and dip to the S at 55–65° or N at 15–45°. The vein groups within each segment all intersect above the top of the buried granite pluton. Steeply dipping veins are most common in the Upper Maoping segment, whereas gently dipping veins can mainly be found in the Lower Maoping and Gaoqiaoxia segments.

The greisen-type W-Sn orebodies (Figure 3) rest at the top of the buried granite pluton and cover an area of ~0.7 km². The orebodies range from hundreds of meters to more than thousand meters long and several meters to tens of meters thick. These ~E–W trending, layered orebodies are tabular, lenticular, or pod-shaped. Wolframite and cassiterite are disseminated in the greisen (Figure 5C,D) with a high topaz content in the middle and upper parts. There is a high concentration of topaz at the edge of greisen, which is associated with mica. Of note, the greisen-type W-Sn orebodies also contain Nb-Ta mineralization.

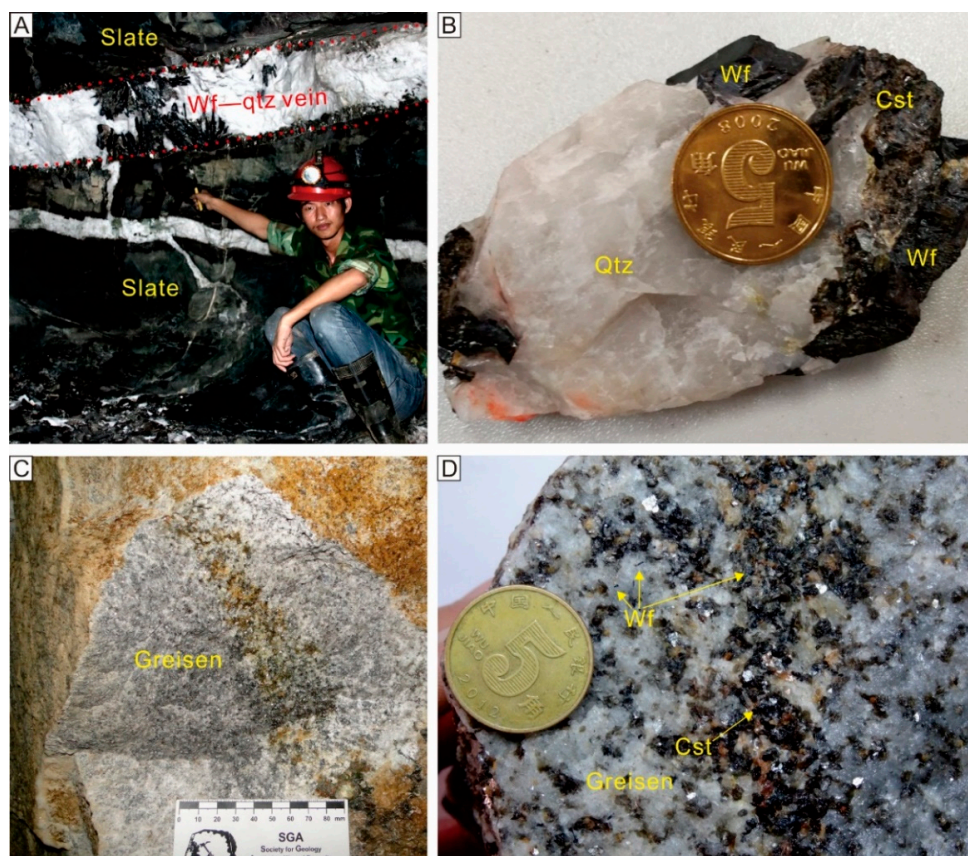


Figure 5. Two types of mineralization in the Maoping W-Sn deposit. (A,B) Quartz vein-type mineralization; (C,D) Greisen-type mineralization. Wf, wolframite; Cst, cassiterite; Qtz, quartz.

4. Samples and Analytical Methods

4.1. LA-ICP-MS Zircon U–Pb Dating

Samples Zk30015–19 (medium–coarse-grained Fe–Li micas granite) and ZK30015–23 (fine-grained Fe–Li micas granite) analyzed in this study for zircon U–Pb dating were collected from drillhole ZK30015, which is located at –5 m elevation of underground tunnel in the 300 exploration line. The drillhole could be mainly divided into three parts: (1) Cambrian metamorphosed sandstone and slate, (2) greisen-type orebodies, (3) medium–coarse-grained Fe–Li micas granite and fine-grained Fe–Li micas granite. Our samples were collected from the third part. Zircon grains for LA-ICP-MS dating were separated from crushed rock samples with a standard technique using an electromagnet and heavy liquids. Then, they were handpicked under a binocular microscope, mounted in an epoxy resin disc and polished down to expose the grain centers. The mounts were photographed with transmitted and reflected lights under a microscope for identifying the analyzed zircon grains (avoiding cracks and inclusions) before vacuum-coating with high-purity gold.

Cathodoluminescence (CL) images of zircon grains were obtained to reveal their internal structures using a JEOL JXA–8100 M electron microprobe equipped with a MonoCL (Gatan, Pleasanton, USA). LA-ICP-MS zircon U–Pb dating was performed using an Agilent 7500a ICP–MS attached to a 213 nm New Wave laser microprobe at the State Key Laboratory for Mineral Deposit Research (MiDeR), Nanjing University (NJU). The detailed analytical processes are similar to those of Jackson et al. [49]. Zircon Mud Tank (intercept age of 732 ± 5 Ma; [50]) was used as an external standard to control reproducibility and instrument stability. Standard zircon GEMOC GJ–1 ($^{207}\text{Pb}/^{206}\text{Pb}$ age of 608.5 ± 1.5 Ma; [49]) was measured twice before and after each run to correct U–Pb fractionation. All of the spot analyses were carried out using a repetition rate of 5 Hz. The laser-ablation beams were 25 μm or 32 μm in diameter

according to the sizes of the zircon grains. U–Pb ages were calculated from the raw signal data using the on-line software package GLITTER (ver. 4.4) [51,52]. Common Pb correction was carried out using the methods of Andersen [53]. Data processing was carried out using Isoplot (version 4.0) [54]. The uncertainties for the isotopic ratios of individual spots are reported at 1 σ , whereas uncertainties for their $^{206}\text{Pb}/^{238}\text{U}$ weighted mean ages are quoted at 2 σ confidence levels.

4.2. LA-ICP-MS Cassiterite U–Pb Dating

Sample Mp-5-11 was collected from the quartz vein in the metamorphosed sandstone at the –5 m mining level. Sample Mp-75-17 was collected from the greisen at the –75 m mining level. Samples were crushed to 40–60 mesh, and cassiterite grains were separated using standard heavy liquid and magnetic techniques. Then, they were handpicked under a binocular microscope, mounted with an in-house external standard cassiterite (Lbiao) in an epoxy resin disc and polished. Based on observations of internal textures under the microscope, inclusion-free cassiterite grains were selected for U–Pb analysis. Cathodoluminescence (CL) images of cassiterite grains were obtained by a Zeiss Supra 55 field emission SEM equipped with a Mono CL4 cathodoluminescence detector at the State Key Laboratory for Mineral Deposit Research (MiDeR), Nanjing University (NJU).

Cassiterite U–Pb dating was carried out using a laser ablation inductively coupled plasma mass spectrometry (LA-ICP-MS) system at the State Key Laboratory of Geological Processes and Mineral Resources (GPMR), China University of Geosciences, Wuhan. The system consists of a Thermal iCAP Qc ICP-MS coupled with a RESOLUTION S—155 193 nm ArF excimer laser. A squid smoothing device was used to reduce the statistical error induced by laser-ablation pulses and to improve the data's quality. Helium gas carrying the ablated sample aerosol was mixed with argon carrier gas and nitrogen as an additional diatomic gas to enhance the sensitivity, before flowing into the ICP-MS. Prior to analysis, the LA-ICP-MS system was optimized using NIST SRM612 ablated with a 50 μm spot size and a 5 $\mu\text{m/s}$ scan speed to achieve maximum signal intensity and a low oxide rate.

Cassiterite grains were analyzed using a laser energy density of 4 J/cm^2 , a spot size of 50 μm and a repetition rate of 10 Hz. An in-lab cassiterite standard (AY-4) was used as an external isotopic calibration standard. AY-4 was collected from the No. 19 skarn orebody in the Anyuan tin deposit of the Furong orefield in Hunan Province, South China. The U–Pb age of the standard cassiterite (AY-4) was established by ID-TIMS as 158.2 ± 0.4 Ma [30]. It also has relatively low common Pb content. Each set of 10 analyses was followed by two measurements of AY-4 and one measurement of NIST SRM 612. Each spot analysis consisted of 30 s of background acquisition, 40 s of data acquisition, 60 s of cleaning the sample cell and plumbing lines. Isotopes were measured in time-resolved mode. For U–Pb dating, the dwell times for each mass scan were 20 ms for ^{238}U , ^{232}Th , ^{208}Pb , ^{206}Pb , and ^{204}Pb and 40 ms for ^{207}Pb . Data processing was conducted by GLITTER (version 4.0) and Isoplot 4.0 [54]. Data uncertainties of the isotopic ratios for individual spots are reported at the 1 σ level, and the errors of their weighted mean $^{206}\text{Pb}/^{238}\text{U}$ ages at the 2 σ level [33].

4.3. Trace Element Concentrations of Cassiterite

A trace element analysis of cassiterite was carried out using an LA-ICP-MS system at the State Key Laboratory for Mineral Deposit Research (MiDeR), Nanjing University (NJU). This system consists of a NexION 350X ICP-MS equipped with a Geolas HD laser. Cassiterite grains were analyzed using a laser energy density of 5 J/cm^2 , a spot size of 44 μm , and a repetition rate of 10 Hz. Helium gas carrying the ablated sample aerosol was mixed with argon as a carrier gas and nitrogen as an additional diatomic gas to enhance the sensitivity before, flowing into the ICP-MS. Each spot analysis incorporated a background acquisition of approximately 20 s followed by 40 s of sample data acquisition. The contents of trace elements for unknown samples were corrected based on the external calibration material NIST SRM 610. ^{118}Sn was used as the internal standard, assuming stoichiometric SnO_2 for quantification purposes. The Sn content of samples was calculated according to the known elementary stoichiometry of cassiterite (SnO_2). Raw data reduction in this study was performed using the GLITTER software.

5. Results

5.1. Zircon U-Pb Ages

LA-ICP-MS zircon U–Pb isotopic analyses were performed on two samples (ZK30015–19 and ZK30015–23) from the Maoping granite rocks. Representative CL images of the separated zircons together with the corresponding U–Pb ages are given in Figure 6. The zircon grains from the medium–coarse-grained Fe–Li micas granite sample (Zk30015–19) are mostly small in size (<150 μm in length), and exhibit a euhedral to subhedral morphology. The Th/U ratios of the analyzed spots vary from 0.37 to 0.95 (Table 1). The CL images for most zircon grains are turbid and dark, but the oscillatory zonings can still be identified (Figure 6A). The zircon grains from fine-grained Fe–Li-micas granite sample (Zk30015–23) are mostly 60–150 μm in length, and exhibit a euhedral to subhedral morphology. The Th/U ratios of the analyzed spots vary from 1.48 to 3.19 (Table 1). The CL images for most zircon grains show clear and bright oscillatory zoning, and some show dark and turbid zoning (Figure 6B). The aforementioned CL image characteristics and Th/U ratios suggest that the analyzed zircon grains are of magmatic origin, without significant later metamorphic overgrowths. The LA-ICP-MS analytical results are presented in Table 1 and illustrated in Figure 7.

Thirteen U–Pb isotope spot analyses on 13 zircon grains were carried out for sample Zk30015–19 (medium–coarse grained Fe–Li-micas granite). One inherited grain shows an older $^{206}\text{Pb}/^{238}\text{U}$ age of 349 ± 6 Ma with low Th and U contents of 563 ppm and 406 ppm, respectively. The Th and U contents for the remaining eight grains fall in the range of 117–1101 ppm and 124–3677 ppm, respectively, with the Th/U ratios varying in the range 0.30–1.49 (Table 1). These spots plot on or near the Concordia, yielding a weighted average $^{206}\text{Pb}/^{238}\text{U}$ age of 159.0 ± 1.5 Ma ($n = 12$; 2σ , MSWD = 0.7) (Figure 7A), represent the crystallization age of the medium–coarse grained Fe–Li-micas granite.

Seventeen U–Pb spot analyses on 17 grains were carried out for sample Zk30015–23 (fine grained Fe–Li-micas granite). The Th and U contents for these analyses fall in the range of 143–915 ppm and 113–289 ppm, respectively, and the Th/U ratios range from 1.48 to 3.19 (Table 1). Two inherited grains yielded an old $^{206}\text{Pb}/^{238}\text{U}$ age of 472 ± 7 Ma and 494 ± 7 Ma. The remaining zircon grains give concordant U–Pb ages, yielding a weighted average $^{206}\text{Pb}/^{238}\text{U}$ age of 125.5 ± 1.3 Ma ($n = 15$; 2σ , MSWD = 1.6) (Figure 7B). The age represents the emplacement age of the fine-grained Fe–Li micas granite.

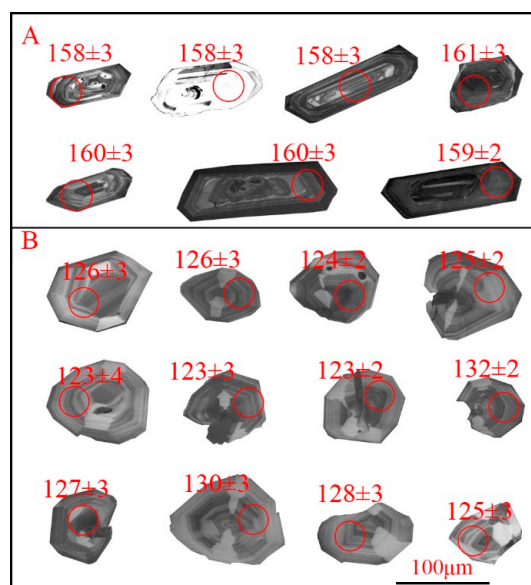


Figure 6. Cathodoluminescence (CL) images and the LA-ICP-MS $^{206}\text{Pb}/^{238}\text{U}$ age of represented zircon grains from the Maoping medium–coarse-grained Fe–Li micas granite (A) and the fine-grained Fe–Li micas granite (B).

Table 1. LA-ICP-MS U–Pb dating results of zircon for granites in the Maoping W–Sn deposit.

Sample Types	Spots	²³² Th (ppm)	²³⁸ U (ppm)	Th/U	Isotopic Ratios						Isotopic Ages (Ma)					
					²⁰⁷ Pb/ ²⁰⁶ Pb	1σ	²⁰⁷ Pb/ ²³⁵ U	1σ	²⁰⁶ Pb/ ²³⁸ U	1σ	²⁰⁷ Pb/ ²⁰⁶ Pb	1σ	²⁰⁷ Pb/ ²³⁵ U	1σ	²⁰⁶ Pb/ ²³⁸ U	1σ
Medium-coarse-grained granite	Zk30015-19-1	832	1181	0.70	0.0505	0.0021	0.1730	0.0073	0.0249	0.0005	217	100	162	6	158	3
	Zk30015-19-2	117	124	0.95	0.0501	0.0033	0.1688	0.0107	0.0244	0.0006	200	150	158	9	156	4
	Zk30015-19-3	616	1296	0.48	0.0492	0.0024	0.1679	0.0079	0.0247	0.0005	159	112	158	7	158	3
	Zk30015-19-4	409	457	0.89	0.0515	0.0016	0.1737	0.0053	0.0245	0.0004	264	73	163	5	156	2
	Zk30015-19-5	563	406	1.39	0.0535	0.0014	0.4095	0.0110	0.0556	0.0009	348	59	349	8	349	6
	Zk30015-19-6	805	1245	0.65	0.0493	0.0015	0.1723	0.0052	0.0253	0.0004	163	73	161	5	161	3
	Zk30015-19-7	568	1322	0.43	0.0493	0.0011	0.1698	0.0039	0.0250	0.0004	164	52	159	3	159	2
	Zk30015-19-8	604	1648	0.37	0.0493	0.0012	0.1708	0.0044	0.0251	0.0004	164	58	160	4	160	3
	Zk30015-19-9	545	1477	0.37	0.0493	0.0017	0.1705	0.0059	0.0251	0.0005	162	82	160	5	160	3
	Zk30015-19-10	586	775	0.76	0.0497	0.0013	0.1684	0.0046	0.0246	0.0004	182	63	158	4	156	3
	Zk30015-19-11	594	707	0.84	0.0498	0.0015	0.1718	0.0052	0.0250	0.0004	186	70	161	4	159	3
	Zk30015-19-12	749	504	1.49	0.0496	0.0012	0.1715	0.0040	0.0251	0.0003	177	56	161	4	160	2
	Zk30015-19-13	1101	3677	0.30	0.0502	0.0007	0.1760	0.0029	0.0254	0.0004	204	33	165	2	162	2
Fine-grained granite	Zk30015-23-1	294	170	1.73	0.0486	0.0036	0.1370	0.0100	0.0205	0.0005	128	168	130	9	130	3
	Zk30015-23-2	167	114	1.47	0.0500	0.0034	0.1365	0.0092	0.0198	0.0005	195	157	130	8	126	3
	Zk30015-23-3	194	113	1.72	0.0486	0.0029	0.1328	0.0076	0.0198	0.0004	130	133	127	7	126	3
	Zk30015-23-4	205	126	1.63	0.0487	0.0024	0.1321	0.0063	0.0197	0.0004	135	110	126	6	125	2
	Zk30015-23-5	239	149	1.60	0.0494	0.0046	0.1312	0.0118	0.0193	0.0006	165	211	125	11	123	4
	Zk30015-23-6	259	154	1.68	0.0509	0.0031	0.1377	0.0083	0.0196	0.0004	235	142	131	7	125	3
	Zk30015-23-7	260	193	1.34	0.0567	0.0012	0.6225	0.0136	0.0797	0.0012	479	46	491	9	494	7
	Zk30015-23-8	331	161	2.06	0.0504	0.0032	0.1310	0.0081	0.0189	0.0004	213	146	125	7	120	3
	Zk30015-23-9	343	169	2.03	0.0491	0.0024	0.1399	0.0067	0.0206	0.0004	155	111	133	6	132	2
	Zk30015-23-10	359	175	2.05	0.0514	0.0027	0.1422	0.0074	0.0201	0.0004	259	125	135	7	128	3
	Zk30015-23-11	143	132	1.08	0.0561	0.0012	0.5881	0.0131	0.0760	0.0011	458	48	470	8	472	7
	Zk30015-23-12	378	213	1.78	0.0497	0.0026	0.1347	0.0070	0.0197	0.0004	181	122	128	6	126	3
	Zk30015-23-13	425	184	2.30	0.0482	0.0021	0.1286	0.0056	0.0193	0.0003	111	99	123	5	123	2
	Zk30015-23-14	464	214	2.17	0.0493	0.0039	0.1349	0.0104	0.0198	0.0006	163	180	128	9	127	3
Zk30015-23-15	559	212	2.63	0.0537	0.0036	0.1420	0.0092	0.0192	0.0005	359	155	135	8	123	3	
Zk30015-23-16	628	254	2.47	0.0489	0.0017	0.1305	0.0046	0.0194	0.0003	141	83	125	4	124	2	
Zk30015-23-17	915	289	3.17	0.0491	0.0016	0.1300	0.0043	0.0192	0.0003	154	79	124	4	123	2	

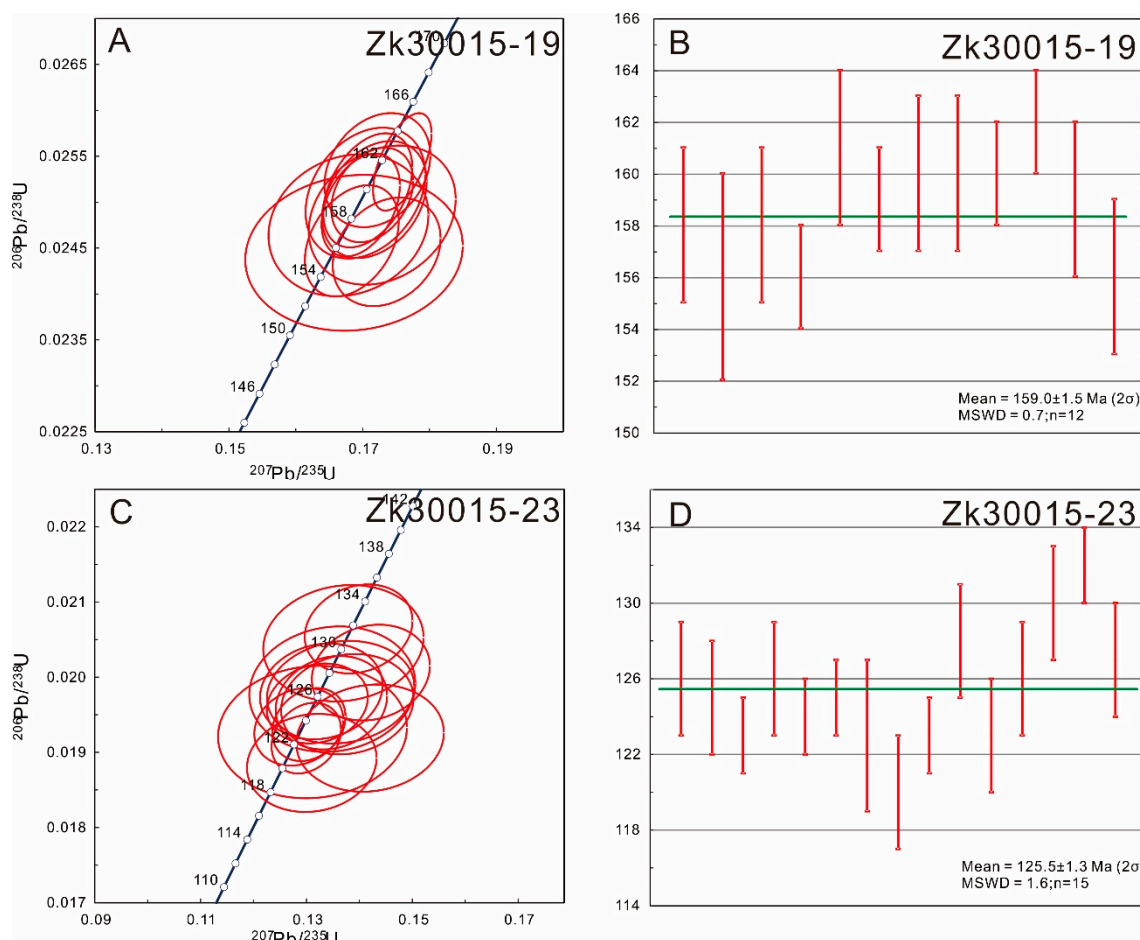


Figure 7. LA-ICP-MS zircon U–Pb concordia plots and weighted mean age diagrams for granites in the Maoping W–Sn deposit.

5.2. Cassiterite U–Pb Ages

LA-ICP-MS cassiterite U–Pb isotopic analyses were performed on two cassiterite samples (Mp-5-11 and Mp-75-17). Representative CL images of the separated cassiterite are given in Figure 8. The cassiterite grains from the quartz vein-type sample (Mp-5-11) are mostly light gray, and all show apparent oscillatory zoning (Figure 8A). The cassiterite grains from the greisen sample (Mp-75-17) are mostly black and dark gray, and show the phenomenon in which the obvious oscillatory zoning area alternates with the inner uniform area (Figure 8B). The LA-ICP-MS analytical results are summarized in Table 2 and illustrated in Figure 9.

Thirty-six spot analyses on 31 cassiterite grains were carried out for sample Mp-5-11 from the quartz vein (Table 2). The cassiterite grains have countable U, but low Th contents. The composition of the 35 ablated spots on the cassiterite grains varies from 0.14 to 4.11 ppm total Pb, <0.10 ppm Th, and 4.9–164 ppm U, respectively. The analytical spots gave a Tera–Wasserburg U–Pb lower intercept age of 157.0 ± 1.3 Ma (2σ , $n = 35$, MSWD = 0.75) (Figure 9A). After ^{207}Pb -based correction, the analyses yielded a weighted mean $^{206}\text{Pb}/^{238}\text{U}$ age of 156.8 ± 1.5 Ma (2σ , $n = 35$, MSWD = 0.59) (Figure 9B), which agrees well with the Tera–Wasserburg U–Pb lower intercept age within error. This indicates that this sample has low common lead content; thus, the age is less influenced and can accurately represent the crystallization age of the cassiterite in the quartz vein.

Thirty-eight analytical spots were measured on 33 cassiterite grains for sample Mp-75-17 from the greisen (Table 2). The cassiterite grains have countable U, but low Th contents. The composition of the 38 ablated spots varies from 0.10 to 2.72 ppm total Pb, <0.33 ppm Th, and 3.2–107.8 ppm U, respectively. The analytical spots gave a Tera–Wasserburg U–Pb lower intercept age of 157.1 ± 1.3 Ma

(2σ , $n = 38$, MSWD = 1.04) (Figure 9C). After ^{207}Pb -based correction, the analyses yielded a weighted mean $^{206}\text{Pb}/^{238}\text{U}$ age of 156.9 ± 1.4 Ma (2σ , $n = 38$, MSWD = 0.81) (Figure 9D), which agrees well with the Tera-Wasserburg U–Pb lower intercept age within error. This indicates that this sample has low common lead content; thus, the age is less influenced and can accurately represent the crystallization age of the cassiterite in the greisen.

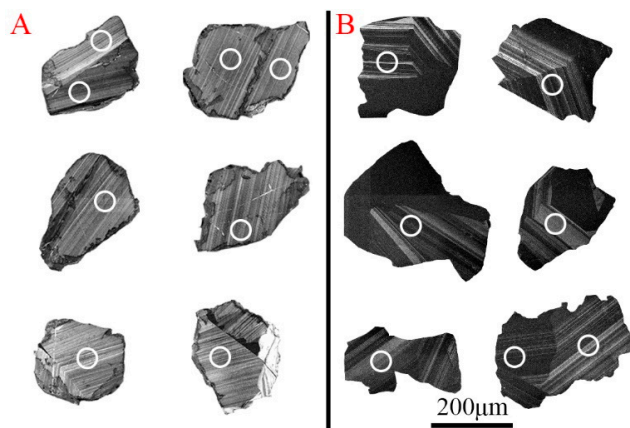


Figure 8. Representative cathodoluminescence images of cassiterite from the Maoping W–Sn deposit. The spot size of the laser beam is 50 μm (white circles). (A) Sample Mp-5-11 from quartz vein ore. (B) Sample Mp-75-17 from greisen ore.

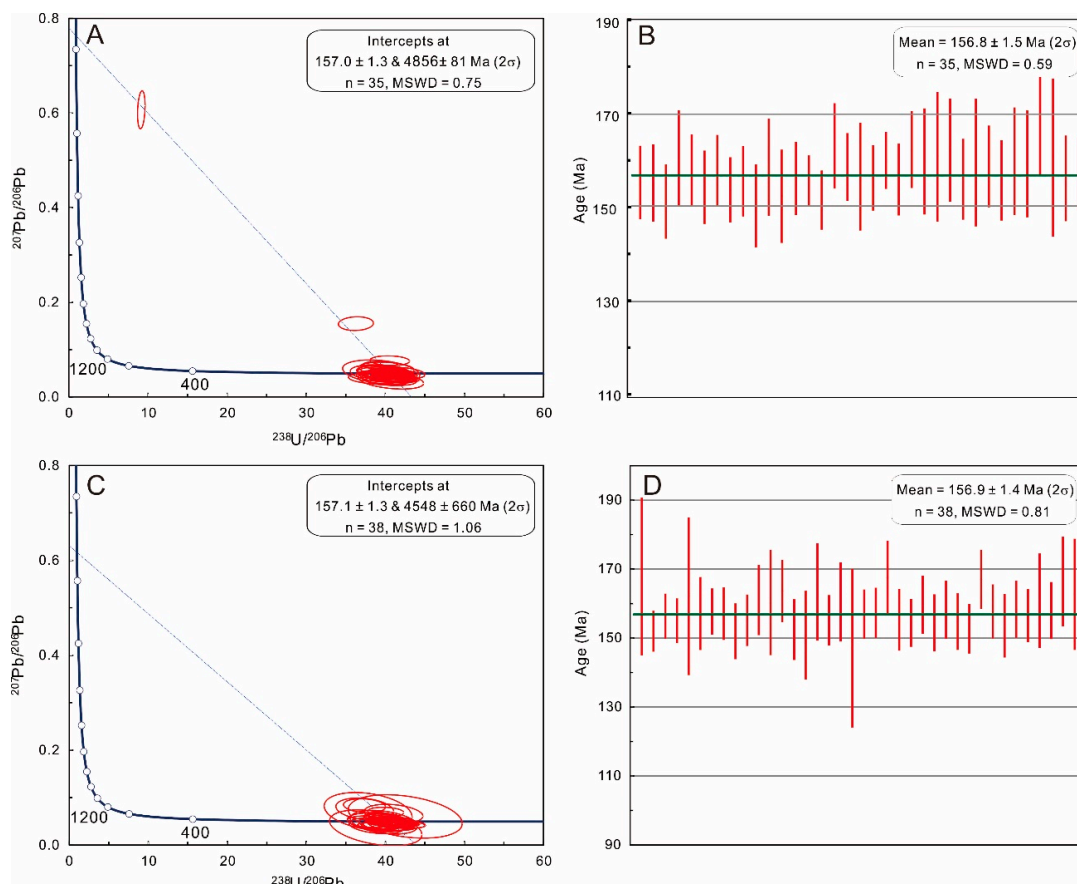


Figure 9. Tera-Wasserburg U–Pb concordia plots and weighted mean $^{206}\text{Pb}/^{238}\text{U}$ age diagrams for cassiterite from the Maoping W–Sn deposit. (A,B) Sample Mp-5-11 from quartz vein ore. (C,D) Sample Mp-75-17 from greisen ore.

Table 2. LA-ICP-MS U–Pb dating results of cassiterite from the Maoping W–Sn deposit.

Sample Types	Spots	Common Pb (ppm)	Total Pb (ppm)	²³² Th (ppm)	²³⁸ U (ppm)	Isotopic Ratios						Isotopic Ages (Ma)	
						²⁰⁷ Pb/ ²⁰⁶ Pb	1 σ	²⁰⁷ Pb/ ²³⁵ U	1 σ	²⁰⁶ Pb/ ²³⁸ U	1 σ	²⁰⁶ Pb/ ²³⁸ U	1 σ
Quartz-vein ore	Mp-5-11-1	0.75	0.63	0.00	25.50	0.04079	0.00378	0.13596	0.01231	0.02410	0.00060	155.3	4.1
	Mp-5-11-2	1.01	0.84	0.00	21.95	0.05013	0.00433	0.16913	0.01416	0.02439	0.00063	155.1	4.3
	Mp-5-11-3	0.71	0.68	0.00	24.25	0.07640	0.00499	0.26053	0.01621	0.02465	0.00062	151.2	4.2
	Mp-5-11-4	1.22	0.37	0.01	13.38	0.05331	0.00579	0.18679	0.01967	0.02533	0.00079	160.4	5.4
	Mp-5-11-5	0.68	0.76	0.00	28.84	0.05261	0.00371	0.18128	0.01237	0.02491	0.00059	157.9	4.0
	Mp-5-11-6	0.67	0.66	0.01	26.06	0.04437	0.00382	0.14767	0.01238	0.02406	0.00060	154.3	4.1
	Mp-5-11-7	0.51	0.82	0.04	28.19	0.06638	0.00419	0.23302	0.01406	0.02537	0.00060	157.8	4.1
	Mp-5-11-8	0.00	1.00	0.01	38.68	0.05120	0.00318	0.17142	0.01027	0.02420	0.00054	153.7	3.7
	Mp-5-11-9	0.71	0.78	0.00	30.93	0.04957	0.00352	0.16752	0.01150	0.02443	0.00058	155.5	4.0
	Mp-5-11-10	1.30	1.02	0.10	25.40	0.15436	0.00742	0.58861	0.02586	0.02756	0.00069	150.3	4.7
	Mp-5-11-11	0.91	0.34	0.00	12.97	0.04296	0.00581	0.14673	0.01940	0.02468	0.00079	158.5	5.4
	Mp-5-11-12	0.84	0.37	0.00	14.33	0.05010	0.00596	0.16594	0.01921	0.02394	0.00076	152.3	5.2
	Mp-5-11-13	0.92	0.74	0.00	28.24	0.04868	0.00375	0.16492	0.01231	0.02449	0.00060	156.1	4.1
	Mp-5-11-14	1.79	4.11	0.01	163.58	0.04438	0.00174	0.14904	0.00570	0.02427	0.00042	155.6	2.9
	Mp-5-11-15	2.85	1.64	0.01	64.02	0.04954	0.00261	0.16310	0.00831	0.02379	0.00049	151.5	3.3
	Mp-5-11-16	0.73	0.53	0.00	20.25	0.04510	0.00404	0.15897	0.01377	0.02547	0.00070	163.1	4.8
	Mp-5-11-17	0.62	1.05	0.00	40.13	0.04474	0.00298	0.15326	0.00988	0.02475	0.00056	158.6	3.8
	Mp-5-11-18	0.69	0.30	0.00	10.72	0.05908	0.00679	0.20365	0.02250	0.02491	0.00089	156.5	6.0
	Mp-5-11-19	0.57	1.17	0.00	45.81	0.04515	0.00286	0.15247	0.00933	0.02440	0.00054	156.3	3.7
	Mp-5-11-20	1.13	3.31	0.00	127.36	0.04257	0.00194	0.14669	0.00648	0.02490	0.00047	160.0	3.2
	Mp-5-11-21	0.97	0.88	0.01	33.30	0.04461	0.00332	0.15016	0.01081	0.02432	0.00059	155.9	4.0
	Mp-5-11-22	0.48	0.81	0.00	31.08	0.03115	0.00316	0.10722	0.01066	0.02487	0.00062	162.2	4.2
	Mp-5-11-23	1.14	0.34	0.00	11.87	0.04969	0.00617	0.17270	0.02080	0.02511	0.00087	159.8	5.9
	Mp-5-11-24	0.58	0.23	0.02	7.91	0.04922	0.00858	0.17202	0.02928	0.02525	0.00105	160.8	7.1
	Mp-5-11-25	0.46	0.36	0.00	13.78	0.04357	0.00574	0.15245	0.01958	0.02528	0.00084	162.2	5.7

Table 2. Cont.

Sample Types	Spots	Common Pb (ppm)	Total Pb (ppm)	²³² Th (ppm)	²³⁸ U (ppm)	Isotopic Ratios				Isotopic Ages (Ma)			
						²⁰⁷ Pb/ ²⁰⁶ Pb	1σ	²⁰⁷ Pb/ ²³⁵ U	1σ	²⁰⁶ Pb/ ²³⁸ U	1σ	²⁰⁶ Pb/ ²³⁸ U	1σ
Quartz-vein ore	Mp-5-11-26	0.68	0.66	0.00	25.82	0.04091	0.00384	0.13710	0.01251	0.02421	0.00066	155.9	4.5
	Mp-5-11-27	1.07	0.21	0.00	7.99	0.03478	0.00815	0.11829	0.02735	0.02457	0.00102	159.5	6.9
	Mp-5-11-28	1.37	0.71	0.00	26.70	0.04022	0.00367	0.13708	0.01213	0.02462	0.00067	158.7	4.6
	Mp-5-11-29	1.72	0.71	0.00	26.67	0.04638	0.00402	0.15635	0.01310	0.02435	0.00066	155.7	4.5
	Mp-5-11-30	1.15	0.32	0.00	12.39	0.03741	0.00612	0.12788	0.02053	0.02470	0.00087	159.8	5.9
	Mp-5-11-31	0.59	0.35	0.00	12.31	0.05309	0.00635	0.18473	0.02135	0.02514	0.00088	159.2	6.0
	Mp-5-11-32	0.76	0.37	0.00	13.77	0.03827	0.00515	0.13780	0.01810	0.02601	0.00086	168.0	5.9
	Mp-5-11-33	0.44	0.14	0.00	4.88	0.05241	0.01172	0.18372	0.04015	0.02533	0.00128	160.6	8.6
	Mp-5-11-34	0.81	0.57	0.00	23.02	0.03845	0.00395	0.12862	0.01283	0.02416	0.00070	156.1	4.8
	Mp-5-11-35	1.04	1.24	0.00	48.69	0.04306	0.00297	0.14583	0.00969	0.02446	0.00060	157.1	4.1
Greisen ore	Mp-75-17-1	1.17	0.11	0.01	3.43	0.03616	0.01650	0.12913	0.05843	0.02579	0.00159	167.8	11.4
	Mp-75-17-2	1.54	2.72	0.01	107.75	0.04306	0.00186	0.14076	0.00595	0.02361	0.00044	152.0	3.0
	Mp-75-17-3	0.98	2.44	0.01	96.17	0.03930	0.00183	0.13136	0.00598	0.02414	0.00046	156.4	3.2
	Mp-75-17-4	0.99	1.69	0.00	64.90	0.04445	0.00234	0.14864	0.00763	0.02414	0.00049	155.0	3.2
	Mp-75-17-5	1.13	0.11	0.00	3.36	0.07055	0.01836	0.25838	0.06558	0.02644	0.00159	162.1	11.4
	Mp-75-17-6	1.42	0.37	0.02	13.28	0.04395	0.00610	0.14883	0.02024	0.02445	0.00078	157.1	5.3
	Mp-75-17-7	2.15	1.85	0.00	70.97	0.04170	0.00223	0.14124	0.00736	0.02445	0.00049	157.7	3.3
	Mp-75-17-8	1.52	1.07	0.00	39.76	0.05609	0.00340	0.19395	0.01135	0.02496	0.00057	157.1	3.8
	Mp-75-17-9	0.99	0.73	0.00	28.77	0.04286	0.00370	0.14022	0.01181	0.02360	0.00060	152.0	4.0
	Mp-75-17-10	1.00	1.01	0.00	39.34	0.04428	0.00305	0.14829	0.00994	0.02416	0.00056	155.2	3.7
	Mp-75-17-11	0.57	0.45	0.00	16.87	0.04073	0.00507	0.14075	0.01718	0.02493	0.00074	161.0	5.1
	Mp-75-17-12	1.05	0.19	0.00	6.43	0.04777	0.01119	0.16638	0.03842	0.02512	0.00110	160.3	7.6
	Mp-75-17-13	0.78	0.63	0.00	23.46	0.04114	0.00385	0.14462	0.01324	0.02535	0.00066	163.6	4.5
	Mp-75-17-14	1.08	0.74	0.00	28.78	0.04345	0.00406	0.14280	0.01298	0.02370	0.00066	152.4	4.4
	Mp-75-17-15	1.50	0.31	0.07	9.68	0.06567	0.00922	0.22197	0.03031	0.02437	0.00090	150.8	6.4

Table 2. Cont.

Sample Types	Spots	Common Pb (ppm)	Total Pb (ppm)	²³² Th (ppm)	²³⁸ U (ppm)	Isotopic Ratios						Isotopic Ages (Ma)	
						²⁰⁷ Pb/ ²⁰⁶ Pb	1σ	²⁰⁷ Pb/ ²³⁵ U	1σ	²⁰⁶ Pb/ ²³⁸ U	1σ	²⁰⁶ Pb/ ²³⁸ U	1σ
Greisen ore	Mp-75-17-16	1.20	0.23	0.04	8.02	0.04757	0.00896	0.16887	0.03119	0.02559	0.00104	163.4	7.1
	Mp-75-17-17	1.11	1.28	0.00	50.20	0.04177	0.00282	0.13944	0.00917	0.02405	0.00054	155.1	3.7
	Mp-75-17-18	0.90	0.32	0.02	12.02	0.04448	0.00652	0.15437	0.02217	0.02500	0.00085	160.5	5.7
	Mp-75-17-19	1.06	0.10	0.00	3.20	0.05988	0.02066	0.19558	0.06619	0.02352	0.00163	147.1	11.5
	Mp-75-17-20	2.34	1.64	0.00	63.04	0.04308	0.00270	0.14593	0.00892	0.02439	0.00053	157.0	3.6
	Mp-75-17-21	1.20	1.46	0.00	55.77	0.04553	0.00293	0.15524	0.00974	0.02455	0.00055	157.3	3.6
	Mp-75-17-22	0.67	0.45	0.03	15.34	0.04874	0.00565	0.17802	0.02012	0.02629	0.00081	167.5	5.4
	Mp-75-17-23	1.14	0.61	0.00	22.67	0.04856	0.00455	0.16429	0.01496	0.02436	0.00068	155.3	4.5
	Mp-75-17-24	0.93	2.12	0.33	83.47	0.04410	0.00273	0.14728	0.00890	0.02403	0.00052	154.4	3.5
	Mp-75-17-25	0.61	0.89	0.00	33.33	0.04791	0.00392	0.16666	0.01329	0.02502	0.00064	159.7	4.2
	Mp-75-17-26	0.80	0.85	0.02	32.56	0.05003	0.00418	0.16894	0.01375	0.02428	0.00063	154.4	4.1
	Mp-75-17-27	1.22	1.16	0.28	41.82	0.05819	0.00414	0.20421	0.01412	0.02524	0.00062	158.2	4.2
	Mp-75-17-28	1.11	0.93	0.02	35.83	0.04605	0.00383	0.15480	0.01256	0.02417	0.00062	154.8	4.1
	Mp-75-17-29	1.73	1.85	0.00	72.81	0.04511	0.00304	0.14937	0.00983	0.02380	0.00054	152.7	3.6
	Mp-75-17-30	0.89	1.36	0.00	52.39	0.03998	0.00307	0.14365	0.01081	0.02583	0.00062	167.0	4.3
	Mp-75-17-31	1.02	2.03	0.06	73.57	0.05741	0.00371	0.20066	0.01266	0.02512	0.00058	157.7	3.9
	Mp-75-17-32	1.38	2.32	0.09	80.87	0.06923	0.00455	0.24074	0.01547	0.02497	0.00058	153.6	4.6
	Mp-75-17-33	1.40	1.22	0.03	45.86	0.04825	0.00387	0.16688	0.01307	0.02483	0.00063	158.4	4.1
	Mp-75-17-34	1.08	1.95	0.00	75.87	0.04491	0.00329	0.15259	0.01095	0.02439	0.00058	156.5	3.8
	Mp-75-17-35	0.60	0.73	0.08	23.06	0.08201	0.00697	0.30594	0.02512	0.02677	0.00078	160.8	6.9
Mp-75-17-36	1.03	1.87	0.27	67.63	0.05756	0.00421	0.20188	0.01442	0.02517	0.00061	158.0	4.1	
Mp-75-17-37	0.85	0.32	0.00	11.38	0.04010	0.00741	0.14384	0.02620	0.02574	0.00094	166.4	6.5	
Mp-75-17-38	1.10	0.30	0.07	8.78	0.07501	0.01084	0.27965	0.03923	0.02674	0.00107	162.7	8.0	

5.3. Trace Elements of Cassiterite

Cassiterite grains from the quartz vein and greisen samples were analyzed for trace elements (Table S1). Overall, the concentrations of trace elements in cassiterite from the Maoping W–Sn deposit are relatively high. Most cassiterite grains are characterized by high concentrations of Nb (25.86–5483 ppm), Ta (72.60–26695 ppm), Zr (67.59–773 ppm) and Hf (26.67–325 ppm). The concentrations of Fe, W, and Ti also vary significantly in all cassiterite grains, with Fe ranging from 145 to 5593 ppm, W ranging from <1 to ~5000 ppm, and Ti ranging from 117 to 3528 ppm. Sc is present at concentrations from 7.9 to 1134 ppm in the cassiterite. The Co and Ni concentrations usually held steady within a single sample. The U concentrations were found to be mostly below 30 ppm. The concentrations of other trace elements are very low (e.g., ≤ 2 ppm Ba, ≤ 2 ppm Mo, ≤ 3 ppm Sb). There are clear positive correlations between Nb and Ta and Zr and Hf, as shown in Figure 10.

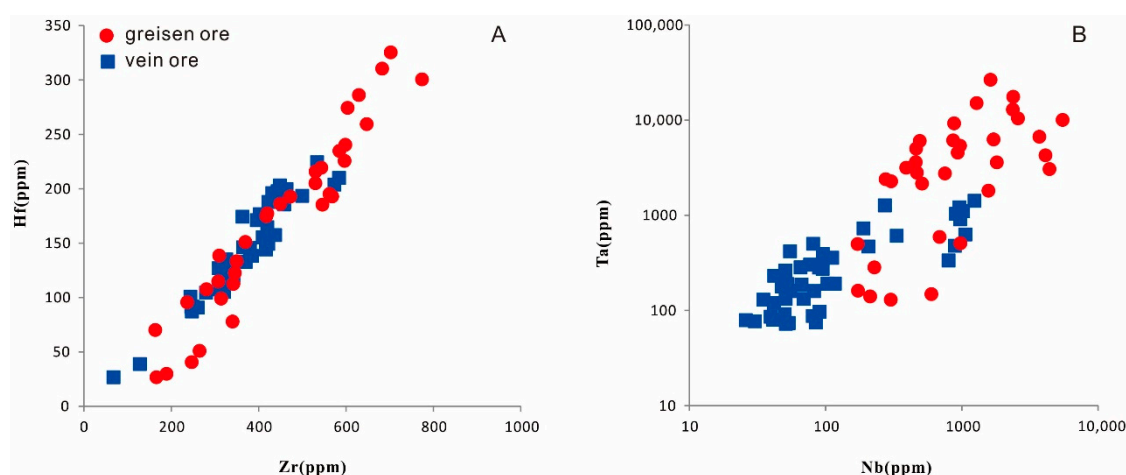


Figure 10. Selected scatterplots of trace elements in the cassiterite samples.

Compared with the cassiterite from quartz vein ores, the cassiterite in the greisen ores contains obviously higher Nb, Ta, Fe, Mn and Sc concentrations, but lower V and Ti concentrations. The Zr and Hf concentrations in the cassiterite from greisen ores are also slightly higher than those in the cassiterite from quartz vein ores. The Zr/Hf ratios of the greisen cassiterite were found to be ~ 3 , which is not much different from those of the quartz vein cassiterite.

6. Discussion

6.1. Mineralization Age of the Maoping W–Sn Deposit

The Gannan metallogenic belt in South China (Figure 1A) is famous for numerous world-class W–Sn polymetallic deposits, dominated by quartz vein-type tungsten deposits [4]. With the progress of deep prospecting work, greisen-type ore bodies in the granite pluton were found at the bottom of some quartz vein-type tungsten ore bodies at, e.g., Huangsha [55], Maoping [56], and Zhangdongkeng [57]. The question of whether there is a genetic relationship between quartz vein- and greisen-type mineralization remains controversial. Xu et al. [14] and Wang et al. [4] emphasized the spatial relationship between the two types of mineralization, but did not determine whether they are the products of the same magma-hydrothermal mineralization event. However, Wei [40] and Hua et al. [16] argued that quartz vein- and greisen-type mineralization are not only spatially associated, but also coeval; moreover, they argued that the two types of mineralization are different forms of the same magma-hydrothermal mineralization event.

As described above, both quartz vein- and greisen-type mineralization developed in the Maoping deposit. In the last few decades, molybdenite Re–Os dating has been used to constrain the W–Sn mineralization ages in the Maoping deposit. Zeng et al. [17] reported a molybdenite Re–Os isochron age

of 156.8 ± 3.9 Ma for the greisen-type mineralization. Li [18] reported a molybdenite Re–Os isochron age of 157.4 ± 2.2 Ma for the quartz vein-type mineralization. Feng et al. [8] reported the molybdenite Re–Os isochron ages of 150.2 ± 2.8 Ma for the quartz vein-type mineralization and 155.3 ± 2.8 Ma for the greisen-type mineralization. The individual ages of the greisen-type mineralization overlap within their analytical errors. However, the dating results of quartz vein-type mineralization are not quite consistent with each other within error. This difference may be caused by the molybdenite from hydrothermal W–Sn deposits having low Re but high common Os contents, and the Re–Os system being occasionally reset by Re loss during the dissolution and/or precipitation reactions of molybdenite [19]. Therefore, it remains unclear whether the two types of W–Sn mineralization are contemporaneous or not based on molybdenite Re–Os ages mentioned above.

Cassiterite, as one of the main ore minerals in a W–Sn deposit, can be used to directly obtain the mineralization ages of W–Sn deposits [21,30]. U–Pb isotope data of cassiterite have previously been shown in $^{206}\text{Pb}/^{207}\text{Pb}$ versus $^{238}\text{U}/^{207}\text{Pb}$ “isochron” plots (e.g., [31]). Recently, Li et al. [33] demonstrated that the Tera–Wasserburg U–Pb lower intercept age is far better for eliminating common Pb effects. In this study, a cassiterite sample collected from a quartz vein-type ore body in metamorphic rock and a cassiterite sample collected from a greisen-type ore body in granite yielded Tera–Wasserburg lower intercept ages of 157.0 ± 1.3 Ma and 157.1 ± 1.3 Ma, respectively. Both of these ages are consistent with their weighted mean $^{206}\text{Pb}/^{238}\text{U}$ ages of 156.8 ± 1.5 Ma and 156.9 ± 1.4 Ma, and each represent the timing of quartz vein-type mineralization and greisen-type mineralization in the Maoping W–Sn deposit. It is obvious that there was only a minimal time difference between the two types of W–Sn mineralization. Therefore, we suggest that the two different types of W–Sn mineralization have a close genetic relationship and were formed during the same magmatic–hydrothermal event in the Maoping deposit. This intimate genetic relationship between the two types of mineralization has also been proved to exist in other tungsten and tin deposits, such as the Zinnwald Sn–W deposit in the Erzgebirge, in which the comparable homogenization temperatures, salinities, and compositions of the ore-forming fluids in the quartz vein and greisen mineralizations suggest that the two types of mineralization are the products of a single parental magmatic–hydrothermal fluid and were formed at roughly the same time [27].

In addition, Peng et al. [58] and Mao et al. [59] pointed out that the most important granite-associated W–Sn polymetallic mineralization in South China took place during the Late Jurassic (160–150 Ma). Our study reveals that the Maoping W–Sn deposit is included in this important W–Sn polymetallic mineralization event in South China. At present, most researchers agree that the subduction of the paleo-Pacific plate played an important role in the formation of the Mesozoic metallogeny and magmatism of South China [7,60–62]. During the Mesozoic period, the Nanling Range was in the southern part of the South China Block, representing an intra-continental setting at ca 160–150 Ma. No arc-related rocks have been found in this area. Hence, we suggest that the Maoping deposit, which is situated in the eastern part of the Nanling region, was developed in an intra-continental setting that was related to the subduction of the paleo-Pacific plate.

6.2. Genetic Relationships between Granitic Magmatism and W–Sn Mineralization

Precise dating of the Maoping granite pluton has been lacking up to now. As mentioned above, the whole-rock Sm–Nd dating was attempted by Li [18], but the result (162 ± 22 Ma) contains considerable uncertainties. The temporal and genetic relationships between the two types of W–Sn mineralization and the Maoping granite pluton remain unclear. The Maoping granite is a hidden pluton located ~4 km to the northeast of the Tianmenshan pluton. The relationship between the Maoping pluton and the Tianmenshan pluton has not been conclusively established, but the Maoping pluton is generally thought to be the northeast-plunging extension of the Tianmenshan pluton [8,18]. As, to date, no precise dating result on the Maoping pluton has been available, the age of ore-forming granite mostly been inferred from the zircon U–Pb data on the Tianmenshan granite. The SHRIMP zircon U–Pb ages of the Tianmenshan granite intrusion were previously determined to be 167 ± 5 Ma for medium–fine-grained

porphyritic biotite granite, 157.2 ± 2.2 Ma for medium-coarse-grained biotite granite, and 151.8 ± 2.9 Ma for porphyritic biotite monzogranite [8,63]. From this time gap and the obvious differences in these granites' mineral assemblages and mineral grain sizes, it is difficult to envisage that the emplacement of these granites was the product of the same intrusive activity. The differences in the three ages indicate that the Tianmenshan granite intrusion event had multiple stages (or episodes), unless the SHRIMP U–Pb ages are biased.

Given that the duration of a hydrothermal system is generally less than 1–2 My [9,64–66], it is considered unlikely that the hydrothermal fluids that evolved in all three intrusion stages are responsible for the ore formation in the Maoping W–Sn deposit. Combined with the molybdenite Re–Os ages, Zeng et al. [17] suggested that greisen-type mineralization is associated with the early stage granite of the Tianmenshan composite granitic pluton; i.e., medium-fine-grained porphyritic biotite granite (167 ± 5 Ma). However, Feng et al. [8] argued that both the greisen-type mineralization and quartz vein-type mineralization are associated with highly differentiated and evolved late-stage granite of the Tianmenshan composite granitic pluton; i.e., porphyritic biotite monzogranite (151.8 ± 2.9 Ma).

In this study, we used LA-ICP-MS zircon U–Pb techniques to directly date the Maoping pluton. The results suggest that the Maoping pluton comprises two main intrusive stages: the medium-coarse-grained Fe–Li micas granite at 159.0 ± 1.5 Ma and the fine-grained Fe–Li micas granite at 125.5 ± 1.3 Ma. Obviously, the age of 159.0 ± 1.5 Ma defined by our new data coincides well with the emplacement timing of the Tianmenshan medium-coarse-grained biotite granite (157.2 ± 2.2 Ma) [8] and the abovementioned W–Sn mineralization ages in the Maoping deposit. Clearly, both the greisen-type mineralization and quartz vein-type mineralization are not only spatially associated but also coeval with the Maoping medium-coarse-grained Fe–Li micas granite.

6.3. Growth Environment of Cassiterite

Cassiterite has a tetragonal lattice structure similar to that of rutile, with Sn^{4+} ions in six-fold coordination with oxygen. Because of its rutile-type structure, cassiterite can incorporate a wide range of trace elements, such as Nb, Ta, Zr, Hf, Ti, W, U, Fe, Sc, V, and Mn [24,34,67]. Some of these elements in cassiterite can be applied as effective indicators of the source fluid composition and formation environment [34,68–70]. Most of the world's tin deposits are spatially and genetically related to granite. However, minor tin deposits also developed in volcanogenic massive sulfide (VMS) and sedimentary-exhalative (SEDEX) systems. Compared with the cassiterite from SEDEX/VHMS deposits, granite-affiliated cassiterite generally contains a much higher amount of Fe and W, which indicates that Fe and W are effective discriminant factors [70,71]. The cassiterites from both the quartz vein mineralization and the greisen mineralization in the Maoping deposit are characterized by elevated Fe and W and fall within the field of granite-related Sn deposits in the Fe versus W binary discrimination plot (Figure 11). In addition, cassiterite from granite-affiliated Sn deposits may contain significant amounts of Nb, Ta, and Zr [6,70,71]. The cassiterites from both the quartz vein mineralization and the greisen mineralization from the Maoping deposit are similar to those from granite-related Sn deposits, as reflected in the high Fe + W + Ta + Zr contents. The Zr/Hf ratios of cassiterite from the Maoping deposit are very low (~ 2.6 in quartz vein and ~ 2.9 in greisen) (Figure 10A). Zr and Hf have a similar ionic charge and ionic radii, and therefore maintain a relatively constant near-chondritic Zr/Hf ratio of 35–40 in most geological systems [72]. Rare cases of significant deviation in this ratio occur in some hydrothermal and highly evolved granites. This indicates that magma activity affected the Maoping deposit's formation process greatly and the ore-forming fluid should be derived from a highly evolved granitic magma.

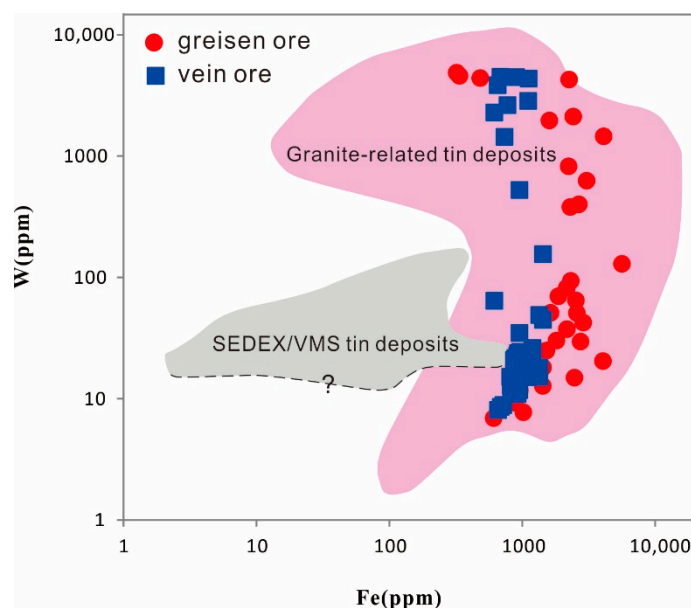


Figure 11. Binary plot of Fe versus W contents in cassiterite from the Maoping W–Sn deposit (modified from [70,71]).

The most abundant trace elements in the cassiterite from the Maoping W–Sn deposit are Nb, Ta, Fe, Ti, Zr, and Hf. Among them, Ti, Zr, and Hf, as the quadrivalent elements, can substitute directly for Sn^{4+} without any charge balance considerations. Nb and Ta occur as 5+ ions, while Fe can be divalent or trivalent. From the covariation plot of Nb + Ta with Fe + Mn (Figure 12B), a few cassiterites from greisen have a relatively higher Nb + Ta concentration with a (Nb + Ta)/(Fe + Mn) ratio of 1:1, corresponding to the coupled substitution: $2\text{Sn}^{4+} = (\text{Nb}, \text{Ta})^{5+} + (\text{Fe}, \text{Mn})^{3+}$. However, we observe a significant excess of Fe cations in all quartz-vein cassiterites and most greisen cassiterites, which means that there needs to be an additional mechanism to incorporate Fe cations. We favour the coupled substitution: $\text{Fe}^{3+} + \text{OH}^- = \text{Sn}^{4+} + \text{O}^{2-}$, as previously proposed [73–75].

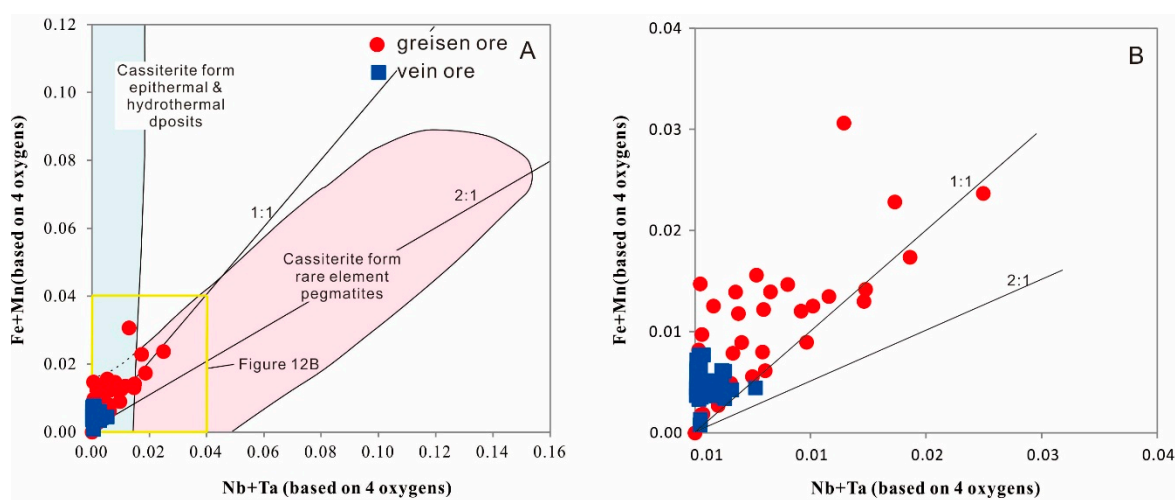


Figure 12. Covariation plot of Nb + Ta with Fe + Mn in cassiterite grains from the Maoping W–Sn deposit (modified from [76]). (B) is the yellow box area of (A).

Cassiterite can form at any stage of magmatic crystallization, and different genetic types of cassiterite have different chemical compositions. Previous studies suggest that magmatic cassiterite related to highly fractionated Li–F granite and pegmatite has elevated Nb and Ta contents with Nb + Ta and Fe + Mn predominantly varying in the ratio of 2:1, but sometimes also in the ratio of 1:1, whereas

hydrothermal cassiterite has low Nb and Ta contents (Figure 12A) [76]. Therefore, in the Maoping deposit, all quartz vein cassiterites and most greisen cassiterites are hydrothermal cassiterite, while a few cassiterites from greisen are magmatic cassiterite as reflected in the concentration of Nb and Ta and the ratio of $(\text{Nb} + \text{Ta})/(\text{Fe} + \text{Mn})$.

Nb and Ta have been suggested as favouring a high-temperature system and Ti as favouring a lower-temperature system [34,68]. In the Maoping deposit, the relatively high Ti, and low Nb + Ta, content of the quartz-vein ore cassiterite implies that this cassiterite crystallized at a relatively lower temperature, whereas the low Ti and high Nb + Ta greisen ore cassiterite formed at a high temperature.

7. Conclusions

(1). LA-MC-ICP-MS cassiterite U–Pb dating of quartz vein and greisen yielded W–Sn mineralization ages of 156.8 ± 1.5 Ma and 156.9 ± 1.4 Ma, respectively, which proved that the two different types of W–Sn mineralization were formed roughly at the same time.

(2). LA-MC-ICP-MS zircon U–Pb dating of the medium-coarse-grained Fe–Li micas granite defines the emplacement age of the Maoping pluton to be 159.0 ± 1.5 Ma. The close agreement between the igneous zircon and the hydrothermal cassiterite indicates a close genetic relationship between the W–Sn mineralization and the Maoping granitic magmatism.

(3). The elevated Fe, Ta and Zr contents in the cassiterite and the low Zr/Hf ratio suggest that the Maoping ore-forming fluid is derived from a highly evolved granitic magma. The cassiterite from greisen ores contains higher Nb, Ta, and Fe contents, but a lower Ti content, than the cassiterite from the quartz vein ores. This indicates that the formation temperature of the greisen-type mineralization is a little higher than that of the quartz vein-type mineralization.

Supplementary Materials: The following are available online at <http://www.mdpi.com/2075-163X/9/7/411/s1>, Table S1: Trace element compositions (ppm) of cassiterite by LA-ICP-MS in the Maoping W–Sn deposit.

Author Contributions: Field work, L.-L.C., W.-S.L.; experiment, L.-L.C., W.-S.L., Z.C.; data analysis, L.-L.C., P.N., B.-Z.D., Z.C., J.-Y.P.; writing—original draft preparation, L.-L.C.; writing—review and editing, L.-L.C., P.N., B.-Z.D., J.-Y.P.

Funding: This work is financially supported by a Key Project of National Nature Science Foundation of China (Grant No. 41830426), a National Key R&D Program of China (Grant No. 2016YFC0600205).

Acknowledgments: The authors thank F.M.S, W.T., L.Z. and Z.X. from Nanjing University and L.M.Y and X.D.W. from the Maoping deposit in South Jiangxi province for their help during fieldwork. We would like to acknowledge Z.K.D and N.P.C from the State Key Laboratory of Geological Processes and Mineral Resources (GPMR), China University of Geosciences, Wuhan for LA-MC-ICP-MS cassiterite dating. Thanks to the State Key Laboratory for Mineral Deposit Research, Nanjing University for their assistance the experiment.

Conflicts of Interest: The authors declare no conflict of interest.

References

1. Anderson, C.S. *Tin*. *USGS 2013 Minerals Yearbook*; Department of the Interior U.S. Geological Survey: Reston, WV, USA, 2015; pp. 77.71–77.79.
2. Shedd, K.B. *Tungsten*. *USGS 2013 Minerals Yearbook*; Department of the Interior U.S. Geological Survey: Reston, WV, USA, 2015; pp. 79.20–79.71.
3. Wang, D.H.; Chen, Y.C.; Chen, Z.H.; Liu, S.B.; Xu, J.X.; Zhan, J.J.; Zeng, Z.L.; Chen, F.W.; Li, H.Q.; Cuo, G.L. Assessment on mineral resource in Nanling region and suggestion for further prospecting. *Acta Geol. Sin.* **2007**, *81*, 882–890. (In Chinese with English abstract)
4. Wang, D.H.; Tang, J.X.; Ying, L.J.; Chen, Z.H.; Xu, J.X.; Zhang, J.J.; Li, S.R.; Zeng, Z.L. Application of “Five levels + Basement” model for prospecting deposits into depth. *J. Jilin Univ. (Earth Sci. Ed.)* **2010**, *40*, 733–738. (In Chinese with English abstract)
5. Romer, R.L.; Kroner, U. Phanerozoic tin and tungsten mineralization—Tectonic controls on the distribution of enriched protoliths and heat sources for crustal melting. *Gondwana Res.* **2016**, *31*, 60–95. [[CrossRef](#)]
6. Taylor, R.G. *Geology of Tin Deposits*; Elsevier: Amsterdam, The Netherlands, 1979; p. 372.

7. Mao, J.W.; Cheng, Y.B.; Chen, M.H.; Franco, P. Major types and time-space distribution of Mesozoic ore deposits in South China and their geodynamic settings. *Miner. Depos.* **2013**, *48*, 267–294. [[CrossRef](#)]
8. Feng, C.Y.; Zeng, Z.L.; Zhang, D.Q.; Qu, W.J.; Du, A.D.; Li, D.X.; She, H.Q. SHRIMP zircon U–Pb and molybdenite Re–Os isotopic dating of the tungsten deposits in the Tianmenshan-Hongtaoling W–Sn orefield, southern Jiangxi Province, China, and geological implications. *Ore Geol. Rev.* **2011**, *43*, 8–25. [[CrossRef](#)]
9. Zhang, R.Q.; Lu, J.J.; Lehmann, B.; Li, C.Y.; Li, G.L.; Zhang, L.P.; Guo, J.; Sun, W.D. Combined zircon and cassiterite U–Pb dating of the Piaotang granite-related tungsten–tin deposit, southern Jiangxi tungsten district, China. *Ore Geol. Rev.* **2017**, *82*, 268–284. [[CrossRef](#)]
10. Bai, X.J.; Wang, M.; Jiang, Y.D.; Qiu, H.N. Direct dating of tin–tungsten mineralization of the Piaotang tungsten deposit, South China, by $^{40}\text{Ar}/^{39}\text{Ar}$ progressive crushing. *Geochim. Et Cosmochim. Acta* **2013**, *114*, 1–12. [[CrossRef](#)]
11. Mao, J.W.; Xie, G.Q.; Guo, C.L.; Chen, Y.C. Large-scale tungstentinn mineralization in the Nanling region, South China: Metallogenic ages and corresponding geodynamic processes. *Acta Petrol. Sin.* **2007**, *23*, 2329–2338. (In Chinese with English abstract)
12. Guo, C.L.; Mao, J.W.; Bierlein, F.; Chen, Z.H.; Chen, Y.C.; Li, C.B.; Zeng, Z.L. SHRIMP U–Pb (zircon), Ar–Ar (muscovite) and Re–Os (molybdenite) isotopic dating of the Taoxikeng tungsten deposit, South China Block. *Ore Geol. Rev.* **2011**, *43*, 26–39. [[CrossRef](#)]
13. Hu, R.Z.; Wei, W.F.; Bi, X.W.; Peng, J.T.; Qi, Y.Q.; Wu, L.Y.; Chen, Y.W. Molybdenite Re–Os and muscovite $^{40}\text{Ar}/^{39}\text{Ar}$ dating of the Xihuashan tungsten deposit, central Nanling district, South China. *Lithos* **2012**, *150*, 111–118. [[CrossRef](#)]
14. Xu, J.X.; Zeng, Z.L.; Wang, D.H.; Chen, Z.H.; Liu, S.B.; Wang, C.H.; Ying, L.J. A new type of tungsten deposit in southern Jiangxi and the new model of “five floors + basement” for prospecting. *Acta Geol. Sin.* **2008**, *82*, 880–887. (In Chinese with English abstract)
15. Wang, D.S.; Lu, S.M.; Hu, B.Y. The geological characteristics and mineralization model of a tungsten-tin deposit. *China Tungsten Ind.* **2011**, *26*, 6–11. (In Chinese with English abstract)
16. Hua, R.M.; Wei, X.L.; Wang, D.S.; Guo, J.S.; Huang, X.E.; Li, G.L. A new metallogenic model for Tungsten Deposit in South China’s Nanling area: Up Veins + Underneath mineralized granite. *China Tungsten Ind.* **2015**, *30*, 16–23. (In Chinese with English abstract)
17. Zeng, Z.L.; Zhang, Y.Z.; Zhu, X.P.; Chen, Z.H.; Wang, C.H.; Qu, W.J. Re–Os isotopic dating of molybdenite from the Maoping tungsten-tin deposit in chongyi county of southern Jiangxi province and its geological significance. *Rock Miner. Anal.* **2009**, *28*, 209–214. (In Chinese with English abstract)
18. Li, G.L. The Evolution of Yanshanian granite and Tungsten mineralization in Southern Jiangxi Province and Adjacent region. Ph.D. Thesis, Nanjing University, Nanjing, China, May 2011.
19. Mccandless, T.E.; Ruiz, J.; Campbell, A.R. Rhenium behavior in molybdenite in hypogene and near-surface environments: Implications for Re–Os geochronometry. *Geochim. Cosmochim. Acta* **1993**, *57*, 889–905. [[CrossRef](#)]
20. Farmer, G.L.; DePaolo, D.J. Nd and Sr isotope study of hydrothermally altered granite at San Manuel, Arizona: Implications for element migration paths during the formation of porphyry copper ore deposits. *Econ. Geol.* **1987**, *82*, 1142–1151. [[CrossRef](#)]
21. Gulson, B.L.; Jones, M.T. Cassiterite: Potential for direct dating of mineral deposits and a precise age for the Bushveld Complex granites. *Geology* **1992**, *20*, 355–358. [[CrossRef](#)]
22. Yuan, S.D.; Peng, J.T.; Hu, R.Z.; Li, H.M.; Shen, N.P.; Zhang, D.L. A precise U–Pb age on cassiterite from the Xianghualing tin-polymetallic deposit (Hunan, South China). *Miner. Depos.* **2008**, *43*, 375–382. [[CrossRef](#)]
23. Jiang, S.Y.; Yu, J.M.; Lu, J.J. Trace and rare-earth element geochemistry in tourmaline and cassiterite from the Yunlong tin deposit, Yunnan, China: Implication for migmatitic-hydrothermal fluid evolution and ore genesis. *Chem. Geol.* **2004**, *209*, 193–213. [[CrossRef](#)]
24. Plimer, I.R.; Lu, J.; Kleeman, J.D. Trace and rare earth elements in cassiterite—Sources of components for the tin deposits of the Mole Granite, Australia. *Miner. Depos.* **1991**, *26*, 267–274. [[CrossRef](#)]
25. Zhang, D.L.; Peng, J.T.; Hu, R.Z.; Yuan, S.D.; Zhang, D.S. The Closure of U–Pb isotope system in cassiterite and its reliability for dating. *Geol. Rev.* **2011**, *57*, 549–554. (In Chinese with English Abstract)
26. Wang, X.D.; Ni, P.; Yuan, S.D.; Wu, S.H. Fluid inclusion studies on coexisting cassiterite and quartz from the Piaotang tungsten deposit, Jiangxi Province, China. *Acta Geol. Sin.* **2013**, *87*, 850–859. (In Chinese with English abstract)

27. Korges, M. Depressurization and boiling of a single magmatic fluid as a mechanism for tin-tungsten deposit formation. *Geology* **2017**, *46*, 75–78. [[CrossRef](#)]
28. Campbell, A.R.; Panter, K.S. Comparison of fluid inclusions in coexisting (cogenetic?) wolframite, cassiterite, and quartz from St. Michael's Mount and Cligga Head, Cornwall, England. *Geochim. Cosmochim. Acta* **1990**, *54*, 673–681. [[CrossRef](#)]
29. Liu, L.J.; Zhou, T.F.; Zhang, D.Y.; Yuan, F.; Liu, G.X.; Zhao, Z.C.; Sun, J.D.; White, N. S isotopic geochemistry, zircon and cassiterite U–Pb geochronology of the Haobugao Sn polymetallic deposit, southern Great Xing'an Range, NE China. *Ore Geol. Rev.* **2017**, *93*, 168–180. [[CrossRef](#)]
30. Yuan, S.D.; Peng, J.T.; Hao, S.; Li, H.M.; Geng, J.Z.; Zhang, D.L. In situ LA-MC-ICP-MS and ID-TIMS U–Pb geochronology of cassiterite in the giant Furong tin deposit, Hunan Province, South China: New constraints on the timing of tin-polymetallic mineralization. *Ore Geol. Rev.* **2011**, *43*, 235–242. [[CrossRef](#)]
31. Zhang, R.Q.; Lu, J.J.; Wang, R.C.; Yang, P.; Zhu, J.C.; Yao, Y.; Gao, J.F.; Li, C.; Lei, Z.H.; Zhang, W.L. Constraints of in situ zircon and cassiterite U–Pb, molybdenite Re–Os and muscovite $^{40}\text{Ar}/^{39}\text{Ar}$ ages on multiple generations of granitic magmatism and related W–Sn mineralization in the Wangxianling area, Nanling Range, South China. *Ore Geol. Rev.* **2015**, *65*, 1021–1042. [[CrossRef](#)]
32. Zhang, R.Q.; Lehmann, B.; Seltmann, R.; Sun, W.D.; Li, C.Y. Cassiterite U–Pb geochronology constrains magmatic-hydrothermal evolution in complex evolved granite systems: The classic Erzgebirge tin province (Saxony and Bohemia). *Geology* **2017**, *45*, 1095–1098. [[CrossRef](#)]
33. Li, C.Y.; Zhang, R.Q.; Ding, X.; Ling, M.X.; Fan, W.M.; Sun, W.D. Dating cassiterite using laser ablation ICP-MS. *Ore Geol. Rev.* **2016**, *72*, 313–322. [[CrossRef](#)]
34. Murciego, A.; Sanchez, A.G.; Dusauroy, Y.; Pozas, J.M.M.; Ruck, R. Geochemistry and EPR of cassiterites from the Iberian Hercynian Massif. *Mineral. Mag.* **1997**, *61*, 357–365. [[CrossRef](#)]
35. Zhou, J.C.; Wang, X.L.; Qiu, J.S. Geochronology of Neoproterozoic mafic rocks and sandstones from northeastern Guizhou, South China: Coeval arc magmatism and sedimentation. *Precambrian Res.* **2009**, *170*, 27–42. [[CrossRef](#)]
36. Zhao, J.H.; Zhou, M.F.; Yan, D.P.; Zheng, J.P.; Li, J.W. Reappraisal of the ages of Neoproterozoic strata in South China: No connection with the Grenvillian orogeny. *Geology* **2011**, *39*, 299–302. [[CrossRef](#)]
37. Wang, G.G.; Ni, P.; Zhao, K.D.; Wang, X.L.; Liu, J.Q.; Jiang, S.Y.; Chen, H. Petrogenesis of the Middle Jurassic Yinshan volcanic-intrusive complex, SE China: Implications for tectonic evolution and Cu–Au mineralization. *Lithos* **2012**, *150*, 135–154. [[CrossRef](#)]
38. Zhou, X.M.; Sun, T.; Shen, W.Z.; Shu, L.S.; Niu, Y.L. Petrogenesis of Mesozoic granitoids and volcanic rocks in South China: A response to tectonic evolution. *Episodes* **2006**, *29*, 26–33.
39. Liu, Z.Q. *Metallogenic Forecasting Theory of Vein Type Tungsten Deposits*; Science Press: Beijing, China, 1980; p. 150.
40. Wei, X.L. The metallogenic features and ore-finding potentiality of the Tungsten deposits in South Jiangxi Province. *China Tungsten Ind.* **2012**, *27*, 14–21.
41. Hsu, K.C. Tungsten deposits of southern Kiangsi, China. *Econ. Geol.* **1943**, *38*, 431–474. [[CrossRef](#)]
42. Zeng, Z.L.; Zhu, X.P.; Jian-X, U. Tungsten reserves of Southern Jiangxi Province and prospecting outlook. *China Tungsten Ind.* **2007**, *22*, 16–18. (In Chinese with English abstract)
43. Chen, J.; Wang, R.C.; Zhu, J.C.; Lu, J.J.; Ma, D.S. Multiple-aged granitoids and related tungsten-tin mineralization in the Nanling Range, South China. *Sci. China Earth Sci.* **2013**, *56*, 2045–2055. (In Chinese with English abstract) [[CrossRef](#)]
44. *Assessment for Tungsten Resource of Zhangyuan Mining Corporation in Chongyi County of Jiangxi Province*; JBGMR (Jiangxi Bureau of Geology & Mineral Resources): Nanchang, China, 2005. (Project Report in Chinese)
45. Tanelli, G. Geological setting, mineralogy and genesis of tungsten mineralization in Dayu district, Jiangxi (People's Republic of China): An outline. *Miner. Depos.* **1982**, *17*, 279–294. [[CrossRef](#)]
46. McKee, E.H.; Rytuba, J.J.; Keqin, X. Geochronology of the Xihuashan composite granitic body and tungsten mineralization, Jiangxi Province, South China. *Econ. Geol.* **1987**, *82*, 218–223. [[CrossRef](#)]
47. Giuliani, G.; Li, Y.D.; Sheng, T.F. Fluid inclusion study of Xihuashan tungsten deposit in the southern Jiangxi province, China. *Miner. Depos.* **1988**, *23*, 24–33. [[CrossRef](#)]
48. *Detailed Geological Survey Report of the Maoping W–Sn Deposit in Chongyi County, Jiangxi Province*; No. 2 team of Jiangxi Nonferrous Geological Prospecting: Nanchang, China, 1989. (Project Report in Chinese)

49. Jackson, S.E.; Pearson, N.J.; Griffin, W.L.; Belousova, E.A. The application of laser ablation-inductively coupled plasma-mass spectrometry to in situ U–Pb zircon geochronology. *Chem. Geol.* **2004**, *211*, 47–69. [[CrossRef](#)]
50. Black, L.; Gulson, B. The age of the Mud Tank carbonatite, Strangways range, Northern Territory. *Bmr J. Aust. Geol. Geophys.* **1978**, *3*, 227–232.
51. Griffin, W.L.; Powell, W.J.; Pearson, N.J.; O'Reilly, S.Y. GLITTER: Data reduction software for laser ablation ICP-MS. *Laser Ablation ICP-MS Earth Sci.: Curr. Pract. Outst. issues* **2008**, *40*, 204–207.
52. Welcome to Glitter—Data Reduction Software for the Laser Ablation Microprobe. Available online: <http://www.glitter-gemoc.com/> (accessed on 3 July 2019).
53. Andersen, T. Correction of common lead in U–Pb analyses that do not report 204 Pb. *Chem. Geol.* **2002**, *192*, 59–79. [[CrossRef](#)]
54. Ludwig, K.R. User's manual for Isoplot/Ex version 3.70: A geochronology toolkit for microsoft Excel: No. 4. *Berkeley Geochronological Cent. Spec. Publ.* **2008**, 1–76.
55. Xia, H.Y.; Liang, S.Y. The evolution of Huangsha-Tieshanlong ore-bearing granite and its ree geochemistry. *Geochemica* **1987**, *4*, 330–340.
56. Huang, D.T. Geological characteristics of tungsten-tin deposit in Maoping, Jiangxi province. *China Tungsten Ind.* **1999**, *3*, 23–24. (In Chinese)
57. Xing, S.J.; Chen, D.S.; Li, G.L. Analysis on the vertical distribution in the Zhangdongkeng W-Mo deposit of Jiangxi. *China Tungsten Ind.* **2010**, *25*, 8–12.
58. Peng, J.T.; Hu, R.Z.; Yuan, S.D.; Bi, X.W.; Shen, N.P. The time ranges of granitoid emplacement and related nonferrous metallic mineralization in Southern Hunan. *Geol. Rev.* **2008**, *54*, 617–625. (In Chinese with English abstract)
59. Mao, J.W.; Xie, G.Q.; Guo, C.L.; Yuan, S.D.; Chen, Y.B.; Chen, Y.C. Spatial-temporal distribution of Mesozoic ore deposits in South China and their metallogenic settings. *Geol. J. China Univ* **2008**, *14*, 510–526. (In Chinese with English abstract)
60. Wang, G.G.; Ni, P.; Yao, J.; Wang, X.L.; Zhao, K.D.; Zhu, R.Z.; Xu, Y.F.; Pan, J.Y.; Li, L.; Zhang, Y.H. The link between subduction-modified lithosphere and the giant Dexing porphyry copper deposit, South China: Constraints from high-Mg adakitic rocks. *Ore Geol. Rev.* **2015**, *67*, 109–126. [[CrossRef](#)]
61. Li, Z.X.; Li, X.H. Formation of the 1300 km wide intracontinental orogen and post-orogenic magmatic province in Mesozoic South China: A flat-slab subduction model. *Geology* **2007**, *35*, 179–182. [[CrossRef](#)]
62. Wang, G.G.; Ni, P.; Zhao, C.; Wang, X.L.; Li, P.; Chen, H.; Zhu, A.D.; Li, L. Spatiotemporal reconstruction of Late Mesozoic silicic large igneous province and related epithermal mineralization in South China: Insights from the Zhilingtou volcanic-intrusive complex. *J. Geophys. Res. Solid Earth* **2016**, *121*, 7903–7928. [[CrossRef](#)]
63. Zeng, Q.T.; Mao, J.R.; Zhang, C.L.; Zhao, X.L. The zircon SHRIMP dating and cooling history of tianmenshan pluton in southern jiangxi province and its ore-forming significance. *Bull. Mineral. Petrol. Geochem.* **2007**, *26*, 348–349. (In Chinese with English abstract)
64. Houghton, B.F.; Wilson, C.J.N.; McWilliams, M.O.; Lanphere, M.A.; Weaver, S.D.; Briggs, R.M.; Pringle, M.S. Chronology and dynamics of a large silicic magmatic system: Central Taupo Volcanic Zone, New Zealand. *Geology* **1995**, *23*, 13–16. [[CrossRef](#)]
65. Kent, A.J.R.; McDougall, I. ⁴⁰Ar–³⁹Ar and U–Pb age constraints on the timing of gold mineralization in the Kalgoorlie gold field, Western Australia. *Econ. Geol.* **1995**, *91*, 792–795.
66. Sillitoe, R.H. Erosion and collapse of volcanoes: Causes of telescoping in intrusion-centered ore deposits. *Geology* **1994**, *22*, 945–948. [[CrossRef](#)]
67. Cheng, Y.B.; Spandler, C.; Kemp, A.; Mao, J.; Rusk, B.; Hu, Y.; Blake, K. Controls on cassiterite (SnO₂) crystallization: Evidence from cathodoluminescence, trace-element chemistry, and geochronology at the Gejiu Tin District. *Am. Mineral.* **2019**, *104*, 118–129. [[CrossRef](#)]
68. Steveson, B.G.; Taylor, R.G. Trace element content of some cassiterites from Eastern Australia. *Proc. R. Soc. Qld.* **1973**, *84*, 43–54.
69. Schneider, H.J.; Dulski, P.; Luck, J.; Moller, P.; Villalpando, A. Correlation of trace-element distribution in cassiterites and geotectonic position of their deposits in Bolivia. *Miner. Depos.* **1978**, *13*, 119–122. [[CrossRef](#)]
70. Hennigh, Q.; Hutchinson, R.W. Cassiterite at Kidd Creek: An example of volcanogenic massive sulfide-hosted tin mineralization. *Econ. Geol. Monogr.* **1999**, *10*, 431–440.

71. Guo, J.; Zhang, R.Q.; Li, C.Y.; Sun, W.D.; Hu, Y.B.; Kang, D.M.; Wu, J.D. Genesis of the Gaosong Sn–Cu deposit, Gejiu district, SW China: Constraints from in situ LA-ICP-MS cassiterite U–Pb dating and trace element fingerprinting. *Ore Geol. Rev.* **2018**, *92*, 627–642. [[CrossRef](#)]
72. Hoskin, P.W.O.; Schaltegger, U. The composition of zircon and igneous and metamorphic petrogenesis. *Rev. Miner. Geochem.* **2003**, *53*, 27–62. [[CrossRef](#)]
73. Möller, P.; Dulski, P.; Szacki, W.; Malow, G.; Riedel, E. Substitution of tin in cassiterite by tantalum, niobium, tungsten, iron and manganese. *Geochim. Cosmochim. Acta* **1988**, *52*, 1497–1503. [[CrossRef](#)]
74. Izoret, L.; Marnier, G.; Dusausoy, Y. Caractérisation cristallographique de la cassiterite des gisements d’étain et de tungstène de Galice, Espagne. *Can. Mineral.* **1985**, *23*, 221–231.
75. Pieczka, A.; Golebiowska, B.; Parafiniuk, J. Geochemistry and origin of the cassiterite from Redziny, lower Silesia, Poland. *Mineralogia* **2007**, *38*, 219–230. [[CrossRef](#)]
76. Tindle, A.G.; Breaks, F.W. Oxide minerals of the separation rapids rare-element granitic pegmatite group, northwestern Ontario. *Can. Mineral.* **1998**, *36*, 609–635.



© 2019 by the authors. Licensee MDPI, Basel, Switzerland. This article is an open access article distributed under the terms and conditions of the Creative Commons Attribution (CC BY) license (<http://creativecommons.org/licenses/by/4.0/>).